



1 Responses of estuarine circulation to the morphological evolution in a  
2 convergent, microtidal estuary

3 Rui Zhang<sup>a</sup>, Bo Hong<sup>b</sup>, Lei Zhu<sup>a,c,d</sup>, Wenping Gong<sup>a,c\*</sup>, Heng Zhang<sup>a,c,d</sup>

4 a- School of Marine Sciences, SunYat-sen University, Guangzhou, China, 510275

5 b- School of Civil and Transportation Engineering, South China University of  
6 Technology, Wushan RD., Tianhe District, Guangzhou 510641, China

7 c- Southern Marine Science and Engineering Guangdong Laboratory (Zhuhai), Zhuhai  
8 519000, China

9 d- Pearl River Estuary Marine Ecosystem Research Station, Ministry of Education,  
10 Zhuhai, 519082, China

11

12 **Abstract:**

13 The Huangmaohai Estuary (HE) is a funnel-shaped microtidal estuary in the west  
14 of the Pearl River Delta (PRD) in southern China. Since China's reform and opening up  
15 in 1978, extensive human activities have occurred and greatly changed the estuary's  
16 topography, and modified its hydrodynamics. In this study, we examined the  
17 morphological evolution by analyzing remote sensing data with ArcGIS tools and  
18 studied the responses of hydrodynamics to the changes in topography from 1977 to  
19 2010 by using the Delft3d model. We took the changes in estuarine circulation during  
20 neap tides in dry seasons as an example. The results show that human reclamation  
21 caused a narrowing of the estuary, and channel dredging deepened the estuary. These  
22 human activities changed both the longitudinal and lateral estuarine circulations. The  
23 longitudinal circulation was observed to increase with the deepening and narrowing of  
24 the estuary. The lateral circulation experienced changes in both the magnitude and  
25 pattern. The momentum balance analysis shows that when the depth and width changed  
26 simultaneously, the longitudinal estuarine circulation was modulated by both the

\* Supported by the National Natural Science Foundation of China under contract Nos 51761135021,  
41506102 and 41890851.

\*\* Corresponding author, E-mail:gongwp@mail.sysu.edu.cn



27 channel deepening and width reduction, in which the friction, pressure gradient force,  
28 and advection terms were altered. The analysis of the longitudinal vortex dynamics  
29 indicates that the changes in the vertical shear of the longitudinal flow, lateral salinity  
30 gradient, and vertical mixing were responsible for the change in the lateral circulation.  
31 The changes in water depth are the dominant factor affecting lateral circulation intensity.  
32 This study has implications for sediment transport and morphological evolution in  
33 estuaries heavily impacted by human interventions.

34

35 **Keywords:** Estuarine circulation, Morphological evolution, Huangmaohai Estuary

36

## 37 1. Introduction

38

39 Estuarine circulation, the tidally averaged flow in estuaries including both the  
40 longitudinal and lateral circulations, is the main driving force for the transport of  
41 sediment, pollutants, and other materials, and also one of the primary factors affecting  
42 the ecological environment of estuaries (Kjerfve et al., 1981). Estuarine circulation is  
43 influenced by many factors (Geyer and Maccready, 2014), such as sea-level  
44 fluctuations (Wilson and Filadelfo, 1986), river discharge, tides (Pritchard, 1952), and  
45 winds (Scully et al., 2005; Waterhouse et al., 2013; Geyer and Maccready, 2014; Salles  
46 et al., 2015; Chen et al., 2020a). Topography in an estuary has a significant effect on  
47 the pattern and intensity of the estuarine circulation (Fischer, 1976; Dyer, 1977).  
48 Human activities may change the estuarine topography, leading to changes in the  
49 estuarine circulation and associated material transport. Therefore, a study of the  
50 estuarine circulation and its response to human activities is essential for integrated  
51 management of the development of estuarine resources, and the maintenance of the  
52 estuary's ecological health.

53 Channel deepening by dredging and sand mining is a common practice in the  
54 development and maintenance of navigable channels and resource utilization in  
55 estuaries. Generally speaking, channel deepening can increase the longitudinal



56 estuarine circulation by decreasing the bottom friction and increasing the baroclinic  
57 forcing which is proportional to the water depth (Amin, 1983; Chernetsky et al., 2010;  
58 Winterwerp, 2011). On the other hand, the increase in water depth can also increase the  
59 salt intrusion and decrease the horizontal density gradient, thus reducing the baroclinic  
60 force. Channel deepening also affects estuarine circulation in other ways, such as  
61 increasing the Stokes transport and the associated compensating return flow (Amin,  
62 1983), altering the nonlinear tidal rectification (Li and O'Donnell, 1997), and tidal  
63 asymmetry in mixing between flood and ebb tides (tidal straining) (Simpson, 1990).  
64 Therefore, the effect of channel deepening is an intricate balance between these  
65 reinforcing and/or competing effects. Chant et al. (2018) demonstrated that a relatively  
66 small (15%) increase in water depth can result in a double exchange flow. They  
67 attributed this increase to the increase in horizontal salinity gradient and/or a reduction  
68 in vertical mixing, but they did not give a clear distinction about how these two effects  
69 work together and which is dominant.

70 Change in estuary width is another aspect of topographic change in estuaries and  
71 is mainly caused by reclamation and utilization of salt marshes, construction of coastal  
72 protection structures along the estuarine banks. Change in estuary width generates a  
73 change in the estuarine convergence, and therefore a change in the estuarine circulation.  
74 Burchard et al. (2014) concluded that an increase in the estuarine convergence results  
75 in an enhancement or reduction of the longitudinal estuarine circulation as increased  
76 estuarine convergence can reduce or even reverse the straining-induced circulation,  
77 though the advection-induced circulation is increased. Changes in estuarine width can  
78 also modify the lateral circulation and feedback to the generation of the longitudinal  
79 estuarine circulation through the change in lateral advection (Lacy et al., 2003; Lerczak  
80 and Rockwell Geyer, 2004; Scully et al., 2009; Burchard et al., 2010; Burchard et al.,  
81 2014). Lerczak and Rockwell Geyer (2004) suggested that lateral effects on the  
82 longitudinal estuarine circulation would be stronger in narrower estuaries given a  
83 constant lateral salinity gradient. Schulz et al. (2015) investigated the impact of the  
84 depth-to-width ratio of the estuarine cross-section on the longitudinal estuarine



85 circulation and found that the longitudinal estuarine circulation exhibits a distinct  
86 maximum in medium-wide channels. They diagnosed the mechanisms for such a  
87 phenomenon and attributed it to the sensitivities of the straining- and advection-induced  
88 circulations on the changes in depth-to-width ratio.

89 As revealed by Lerczak and Geyer (2004) and other researchers (Chen et al.,  
90 2020b), lateral processes play important roles in the generation of the longitudinal  
91 estuarine circulation. The lateral circulation can modify the longitudinal estuarine  
92 circulation by the lateral redistribution of the longitudinal current in a direct way  
93 (Lerczak and Geyer, 2004), and change the longitudinal pressure gradient force and the  
94 friction in an indirect way. In estuaries, the pattern and intensity of lateral circulation  
95 are controlled by three processes (Li et al., 2014): vertical shear of the longitudinal  
96 current affecting the tilting of planetary vorticity, lateral salinity gradient (baroclinicity),  
97 and diffusion. The longitudinal estuarine circulation can affect the lateral circulation  
98 through all the mentioned three factors. Therefore, the interaction between the  
99 longitudinal and lateral processes is fully nonlinear and quite complex. Though these  
100 interactions have been discussed in detail (Scully et al., 2009; Li et al., 2017), several  
101 questions remain open: How does the longitudinal estuarine circulation affect the  
102 intensity and vortex structure of the lateral circulation? Does a decreased/increased  
103 lateral circulation necessarily lead to a weakened/strengthened longitudinal circulation?  
104 These questions become complicated in an estuary where both width and depth vary.  
105 Previous studies showed that the narrowing and deepening of the Yangtze River  
106 Estuary resulted in an enhanced longitudinal estuarine circulation (Zhu, 2018), which  
107 changed from transversely sheared to vertically sheared. The estuarine stratification  
108 was also found to be strengthened, along with an increase in the intensity of lateral  
109 circulation. Zhu et al. (2015) investigated the influences of channel deepening and  
110 widening on the tidal and nontidal circulations of Tampa Bay, USA, and found that the  
111 nontidal circulation was strengthened by these human interventions. However, how  
112 does the estuarine circulation respond to both narrowing and deepening/shallowing of  
113 the estuary? What happens when the narrowing rate is much larger or smaller than the



114 deepening rate in an estuary? Here the narrowing rate is the ratio of the difference of  
115 cross-section widths between two consecutive years divided by the width in the earlier  
116 year. Similarly, the deepening rate is the ratio of the difference of water depth in the  
117 cross-section between the two consecutive years divided by the earlier year's depth.

118 Here we try to address the above questions by studying the changes in the estuarine  
119 circulation via using the historical topographic data obtained from 1977 to 2010 in the  
120 Huangmaohai Estuary (HE). The HE is a microtidal estuary in the southwest of the  
121 Pearl River Delta (PRD), and experienced different stages of topographic changes  
122 under human activities from 1977 to 2010, which can be grouped into two scenarios:  
123 narrowing and deepening (1977-1994, and 2003-2010), and narrowing and shallowing  
124 (1994-2003). These two scenarios of topographic changes caused different responses  
125 of the estuarine circulation, and thus provided a good opportunity to study the effect of  
126 human activities induced morphological evolution on the estuarine circulation.

127 In this study, we used a state-of-the-art three-dimensional baroclinic model (Delft  
128 3d) to simulate the changes in hydrodynamics in the HE in different years and examined  
129 the changes in intensities of the longitudinal and lateral estuarine circulations, followed  
130 by an analysis of the mechanisms for these changes by conducting diagnostic analyses  
131 of the momentum balance. The structure of the rest of the paper is as follows. Section  
132 2 introduces the study area and numeral model (including model setting and validation).  
133 Section 3 presents the results of morphological evolution and changes in the estuarine  
134 circulation. Then, the mechanisms for the changes in estuarine circulation are  
135 investigated using the momentum and vortex balance equations in Section 4. Finally,  
136 the conclusions are presented in Section 5. For the sake of conciseness, we append a  
137 supplement in the appendix about the model validation for water level, current, and  
138 salinity.

139

## 140 **2. Study area and methodology**

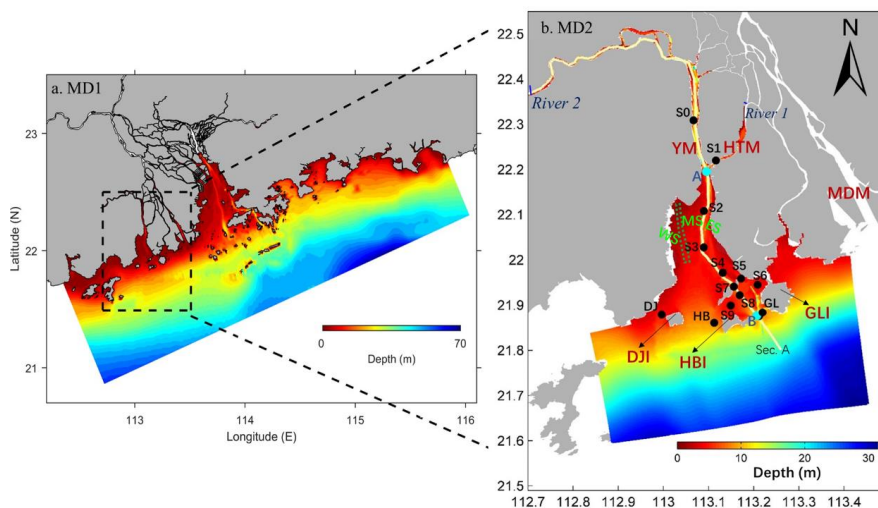
141

### 142 **2.1 Study area**



143

144 The HE is located in the west of the PRD in southern China and exhibits a  
145 distinctly convergent geometry, with a latitude ranging from 21°50' to 22°13' N and  
146 a longitude ranging from 113°00' to 113°51' E (Fig. 1). The estuary is composed of a  
147 bay (Huangmao Bay) and a tidal river. The bay is trumpet-shaped with an area of 409  
148 km<sup>2</sup>. It has a complex bathymetry comprising of two channels and three shoals, namely  
149 the West Channel and East Channel, the West Shoal, Middle Shoal, and East Shoal. In  
150 recent decades, the West Channel is observed to shrink and almost disappear now (Jia  
151 et al., 2012). The width of the bay is 30 km at the estuary mouth and decreases to 1.8  
152 km at the head. The mean water depth of the bay is 4.5 m (Gong et al., 2014). The bay  
153 is connected to the upstream river catchment by two constrictions (Yamen and  
154 Hutiaomen Outlets). Several islands, namely Dajin Island, Hebao Island, and Gaolan  
155 Island, are scattered at the estuary's mouth. The estuary mouth is divided into three  
156 entrances: the West Entrance between the Dajin Island and the western shore; the  
157 Central Entrance between the Dajin Island and the Hebao Island, where the West  
158 Channel passes through; and the East Entrance between the Hebao Island and the  
159 Gaolan Island, where the East Channel goes through (shown in Fig. 1b).



160

161



162 Fig. 1. The study area (Huangmaohai estuary) and observation stations. Major topographic  
163 features and domains of the nested modeling system over (a) the PRD and (b) the HE and its  
164 adjacent waters. YM = Yamen; HTM = Hutiaomen; MDM = Modaomen; DJI = Dajing Island;  
165 GLI = Gaolan Island; HBI = Hebao Island. The black dots (S0–S9, DJ, HB, and GL) in the  
166 MD2 domain are stations of field deployments in March 2010. The solid lines represent the  
167 along-channel transect (Section A (AB)), which lies in the East Channel. The green dotted lines  
168 represent the West Channel in 1977. Three shoals in (b): West Shoal (WS), Middle Shoal (MS),  
169 and East Shoal (ES).

170

171 The HE has a subtropical monsoon climate, with the precipitation in the wet season  
172 (from May to September) being high. Approximately 80% of the river discharge occurs  
173 during the wet season, with an average discharge of 200.23 m<sup>3</sup>/s. The tides in the HE  
174 are mixed semidiurnal with dominant semi-diurnal constituents and smaller diurnal  
175 constituents. The tides show obvious asymmetry in terms of tidal duration, velocity,  
176 and current acceleration between floods and ebbs (Gong et al., 2016). The tidal range  
177 is approximately 1.5 m at the mouth and experiences an initial increase from the mouth  
178 towards the head owing to a strong convergence of the bay width. Further landward in  
179 the tidal river beyond the bay head, the tidal range decreases by the overwhelming  
180 bottom friction (Gong et al., 2012). The tidal current velocity ranges from 0.5 m/s to  
181 1.5 m/s (Huang, 2011), and is higher in deep channels than on shallow shoals. The tidal  
182 currents are generally rectilinear in deep channels but become more rotary in shallow  
183 shoals.

184 Since the 1980s, human activities have been intense in the HE estuary. A  
185 hydroelectric power project upstream of the estuary, channel dredging, sand mining,  
186 and construction of Gaolan Island levees have led to great changes in the HE's  
187 topography. Also, the HE has rich tidal flat resources and endured frequent reclamation  
188 activities. From 1965 to 2003, a total of 142.29 km<sup>2</sup> tidal flat was reclaimed, with an  
189 average reclamation rate of 3.74 km<sup>2</sup>/a, and the reclamation rate continuously but  
190 gradually increased during that period. After 2003, the reclamation rate slowed down.  
191 In terms of channel dredging, the Yamen Waterway Project was conducted in 1997 to  
192 deepen the channel between S0 and S3 in Fig. 1b (Luo, 2010). In April 2005, the Yamen



193 Channel regulation project was implemented to alleviate the serious siltation in the  
194 channel, with the channel being dredged to a depth of about 6 m.

195 In the following, we chose 1977, 1994, 2003, and 2010 as the representative years  
196 to study the typical scenarios of bathymetric changes in the HE.

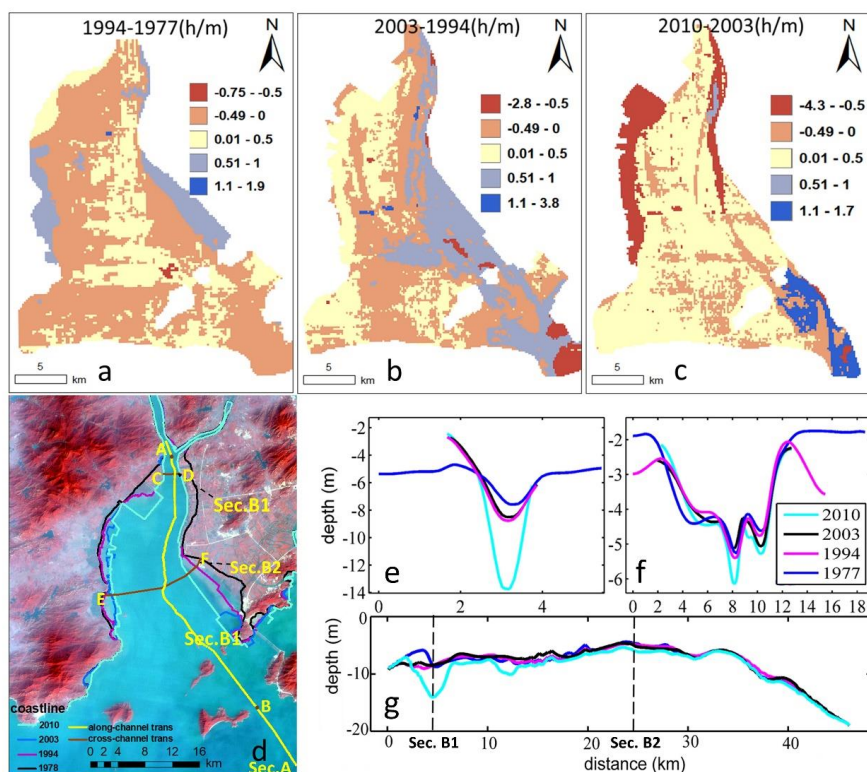
197

## 198 **2.2 Remote sensing and topographic data**

199

200 Remote sensing data were used for coastline extraction and included Landsat  
201 Multi-Spectral Scanner (MSS) data, Landsat Thematic Mapper (TM) data, and Landsat  
202 Operational Land Imager (OLI) data. A total of 142G data of 66 images (Table 1)  
203 covering the PRD during cloudless days in multiple years (from 1973 to 2018) were  
204 downloaded from <http://www.gscloud.cn/>. These data were firstly processed by  
205 geometric and atmospheric corrections by the ENVI 5.3 software. Subsequently, they  
206 were compared with topographic data for further geometric corrections. The errors were  
207 shown to be less than 0.5 pixels (Ai et al., 2019). The topography data inside the HE  
208 were derived from nautical charts (1977, 1994, 2003, and 2010), published by the  
209 Navigation Safety Guarantee Bureau. The filling and excavation toolbox of ArcGIS  
210 was used to calculate the difference between the volumes in two consecutive periods  
211 by superimposing the corresponding Digital Elevation Models (DEM). This method is  
212 actually to decompose three-dimensional space entities into many cuboids, then  
213 calculate the differences of area and volume of each cuboid between two consecutive  
214 years, and classify the cuboids into different categories based on the siltation thickness.  
215 We thus obtained the average siltation rates of the study area over different years (Figs.  
216 2a-c).





217  
 218 Fig. 2. (a-c) Water depth difference between two consecutive years ((a)1994-1977; (b)2003-  
 219 1994; (c)2010-2003), where the positive value indicates “deepening” and the negative one  
 220 indicates “siltation”, (d) Shorelines of 1977-2010 and locations of two cross-sections (AB: Sec.  
 221 A; CD: Sec. B1; EF: Sec. B2); (e, f, and g) The bathymetric evolutions at Sections B1, B2, and  
 222 A in 1977, 1994, 2003, and 2010.

223  
 224  
 225  
 226

Table 1. Data of remote sensing images

Time	Satellite	Image sensor	Resolution/m	Path/Row	Memory space
1973,1978	Landsat3	MSS	78		
1986-2011	Landsat5	TM	30		
2012	Landsat7	ETM	30	122/45	142G
2013-2018	Landsat8	OLR	30		

227  
 228  
 229



### 230 **2.3 Numerical model setting up and validation**

231

232 The numerical model Delft3d was used to simulate the hydrodynamics in the HE.  
233 The Delft3d model is a fully three-dimensional hydrodynamic water quality model, and  
234 can accurately simulate large-scale flow, water quality, and morphological evolution  
235 (Lesser et al., 2004). The algorithm of the Delft3d model can guarantee the conservation  
236 of mass, momentum, and energy. The model grid consisted of a nesting grid system,  
237 with the MD1 (parent model, Fig. 1a) covering the whole PRD, and the MD2 (child  
238 model) covering the HE. For the MD2 model, an orthogonal Cartesian horizontal grid  
239 of 269\*620 was established, with the horizontal resolution ranging from 85 m in the  
240 channel to 324 m at the ocean boundary. Vertically, the grid was discretized into 10  
241 layers of  $\sigma$  coordinate. The model system used here is the same as the one in Chen et  
242 al. (2020a). Briefly, the open boundary conditions of the MD1 model included  
243 atmospheric forcing at the water surface, river discharge at the upstream boundary, tidal  
244 and non-tidal water elevations and currents, a constant salinity of 34 psu at the open  
245 ocean boundary. The results from the MD1 were interpolated to provide ocean  
246 boundary conditions for the MD2 model.

247 As mentioned above, the hydrodynamics in the HE experiences distinct seasonal  
248 variation. The estuarine circulation during the wet season has been extensively studied  
249 before (Chen et al., 2020a; Chen et al., 2020b). Here we choose the dry season to  
250 investigate the changes in the estuarine circulation caused by topographic changes in  
251 different years. We conducted a series of numerical experiments using the bathymetry  
252 data in 1977, 1994, 2003, and 2010. The simulation time was chosen to be from 00:00  
253 on March 1 to 23:00 on March 31 in the dry season, when observation data were  
254 available in 2010. Field measurements were carried out at 14 mooring stations on  
255 March 17th 17:00 to 18th 22:00, 2010. In these surveys, ADCP was utilized to measure  
256 the vertical profile of current with a vertical resolution of 0.3 m and a time resolution  
257 of 5 min, and CTD was used to measure the vertical profiles of salinity and temperature  
258 every hour. Hourly data were obtained after post-processing of the raw data and used



259 for model validation here. In all the four scenarios, two upstream boundaries were  
 260 specified (Fig. 1b): at River 2 by specifying real-time water level data from the MD1  
 261 model from 00:00 on March 1, 2010, to 23:00 on March 31, 2010, with a time interval  
 262 of 1 hour; At River 1 by specifying a constant river discharge of  $100 \text{ ms}^{-2}$ . The choice  
 263 of this constant value was based on the previous simulation experiences (Chen et al.,  
 264 2020a; Chen et al., 2020b). The salinities at the river inflow boundaries were set to be  
 265 0 psu. The only changing condition of the four scenarios was the topography (Table 2),  
 266 so the effect of topographic change can be identified. The measured data from 14  
 267 stations in 2010 were used to validate the model. The validation included water level,  
 268 current direction and magnitude, and salinity (Figs. A. 1-4).

269

270 Table 2. Coastline, bathymetries, salinity, flow, and tidal boundary in the four model scenarios.

Scenario	Coastline	Bathymetrie s	The salinity of the open sea	Flow	Tidal boundary
1977/03	1977	1977	2010/03	2010/03	2010/03
1994/03	1994	1994	2010/03	2010/03	2010/03
2003/03	2003	2003	2010/03	2010/03	2010/03
2010/03	2010	2010	2010/03	2010/03	2010/03

271

272 In this study, the Willmott skill score (SK) was used to evaluate whether the model  
 273 result is consistent with the observed data (Willmott, 1981). The SK is defined as:

$$274 \quad SK = 1 - \frac{\sum_{i=1}^n (O_i - M_i)^2}{\sum_{i=1}^n (|M_i - \bar{o}| + |O_i - \bar{o}|)^2}, \quad (1)$$

275 where  $n$  is the number of the observed data,  $M$  and  $O$  are model simulation results  
 276 and observations, respectively, and  $\bar{o}$  is the average value of the observation data. SK  
 277 is used to measure the consistency between the model results and the observations, with  
 278 a value between 0 and 1. The larger the value is, the more consistent the simulation  
 279 results are with the observed data.

280 Firstly, the water level of the MD2 model was validated (Fig. A. 1). The SKs of the  
 281 four observed stations are all above 0.86, indicating that the water level simulation is  
 282 reasonable. Secondly, the modeled current direction showed good performance except



283 for the surface layer at Stations DJ and S0 (Fig. A. 2), almost all the SKs are greater  
284 than 0.7 (Table 3). The simulation of current speed (Fig. A. 3) is worse than that of the  
285 current direction, but the SKs at most stations are above 0.6, showing a good  
286 performance. We note that the SK (less than 0.4) at Station S3 is significantly lower  
287 than other stations, mostly because the station was located near the null point (the  
288 convergence point between seaward and landward bottom residual flows) and the  
289 current speed was quite small. Lastly, the trends of observed and simulated salinities  
290 are consistent (Fig. A. 4), and almost all the SKs of salinity validation are above 0.5,  
291 especially in S1-S3, showing a good performance of the salinity simulation.

292  
293

Table 3. Skill scores by comparison of modeled results with observations.

Stations	Current direction			Current speed			Salinity		
	Sur	Mid	Bot	Sur	Mid	Bot	Sur	Mid	Bot
S0	0.18	0.96	0.96	0.77	0.88	0.86	0.32	0.35	0.35
S1	0.94	0.99	0.99	0.65	0.66	0.61	0.94	0.94	0.90
S2	0.78	0.79	0.71	0.83	0.84	0.84	0.84	0.85	0.85
S3	0.87	0.98	0.95	0.34	0.38	0.39	0.92	0.79	0.77
S4	0.84	0.94	0.94	0.53	0.55	0.53	0.77	0.64	0.54
S5	0.86	0.92	0.93	0.66	0.71	0.72	0.37	0.25	0.26
S6	0.79	0.90	0.88	0.68	0.75	0.74	0.15	0.20	0.25
S7	0.82	0.85	0.96	0.74	0.79	0.83	0.86	0.66	0.56
S8	0.84	0.89	0.89	0.59	0.62	0.66	0.82	0.77	0.72
S9	0.80	0.74	0.77	0.54	0.46	0.41	0.59	0.50	0.52
DJ	0.61	0.77	0.77	0.38	0.47	0.51	0.66	0.47	0.37
GL	0.89	0.91	0.93	0.50	0.51	0.49	0.37	0.43	0.41
HB	0.71	0.89	0.89	0.60	0.56	0.56	0.57	0.54	0.53

294

295 As a whole, the simulation of surface currents is worse than that in other layers,  
296 since winds and waves were not included in our model simulations, in which the surface  
297 flow is more susceptible to these forcings. The specified river flow at River 2 was  
298 constant, which may deviate from the real-time data (not available), leading to a poor  
299 salinity reproduction at upstream stations. In short, the water level and current are well-  
300 validated. The simulation of salinity is generally good, except for some deviations at  
301 upstream stations. It shows that the model can reasonably simulate the hydrodynamic  
302 processes in the area, and can be used for the following hydrodynamics study in the HE.



303

### 304 **3. Results**

305

#### 306 **3.1 Morphological evolution**

307

308 Morphological changes between 1977, 1994, 2003, and 2010 are shown in Figs.  
309 2a-c. According to the pattern of erosion and siltation in the two consecutive years,  
310 most areas in the HE experienced siltation from 1977 to 1994. The East Channel was  
311 deepened by about 0-0.5 m. In the middle of the bay, the nearshore areas were under  
312 erosion, and the erosion thickness at the eastern shore was twice that at the western  
313 shore. In other areas, the siltation thickness was between 0 and 0.5 m. From 1994 to  
314 2003, erosion occurred in the West Shoal, East Channel, East Shoal, and Middle Shoal.  
315 Siltation of 0.01-0.5 m happened in the rest of the area, which accounted for most of  
316 the HE, so the HE became shallower in 2003. From 2003 to 2010, the West Shoal  
317 became significantly shallower with a siltation thickness of about 0.5-1m. The East  
318 Shoal almost disappeared, and its relict area endured siltation of 1.1-1.7 m, which was  
319 mainly due to the construction of coastal protection works. Strong erosion occurred in  
320 other areas, especially in the upper bay with a deepening of more than 4m, and the  
321 overall water depth of the HE became greater in 2010.

322 We further take the morphological change of the East Channel as an example. The  
323 East Channel experienced continuous erosion before 1977. From 1977 to 2003, the  
324 channel was under siltation, particularly at the river mouth bar (between the upper bay  
325 and the entrances, see Gong et al. (2014), whereas at the upper bay (from the head to  
326 the null point of the East Channel, here the null point means the convergence point at  
327 which the upstream seaward flow meets the downstream landward bottom flow) and at  
328 the inter-island sections, the channel was under erosion. In 2003, siltation in the East  
329 Channel was serious and the water depth there became only 2m (Li, 2019). From 2005



330 on, the East Channel had been under erosion and the largest water depth reached 7.4 m  
331 in 2006 (Luo, 2010).

332 Overall, the water depth of the HE changed considerably from 1977 to 2010. It  
333 first experienced erosion, then underwent siltation, and followed by erosion again.

334 Figure 2d shows the changes of coastlines for the four representative years. To  
335 calculate the rate of geometry convergence, the DSAS tool (Version 5.0) in Arcmap  
336 10.3 was used to calculate the end-point rates for cross-shore transects. A more detailed  
337 procedure is in Zhang et al. (2019). We chose one longitudinal section along the channel  
338 in the estuary and two cross-sections (in Fig. 2d) along the channel for analysis. The  
339 longitudinal section (Sec. A) extends from the bay head (point A in Fig. 1b) to the  
340 estuary mouth (point B in Fig. 1b), spanning a distance of 50 km. Sec. B1 is located at  
341 about 4 km downstream from the bayhead, where the water depth changes sharply in  
342 the lateral (or longitudinal) direction (see Fig. 2e). Sec. B2 is approximately 24km  
343 downstream from the bayhead and near the null point in the middle of the estuary (see  
344 Fig. 2f), and the width of the estuary varied dramatically here (see Fig. 2e). At Sec. A,  
345 the water depth near the point of Sec. B1 endured a great change in 2010 due to channel  
346 dredging (Fig. 2g). In other periods, the water depth along its course endured gradual  
347 deepening. At Sec. B1, the bathymetric change is featured by an increase in water depth  
348 and negligible change in width over time. At Sec. B2, both the water depth and width  
349 experienced changes from 1977 to 2010, with the depth increased and width decreased  
350 (Fig. 2f). The above three sections clearly depict the topographic changes of the estuary  
351 in different years.

352

### 353 **3.2 changes in the vertically averaged flow and salinity**

354

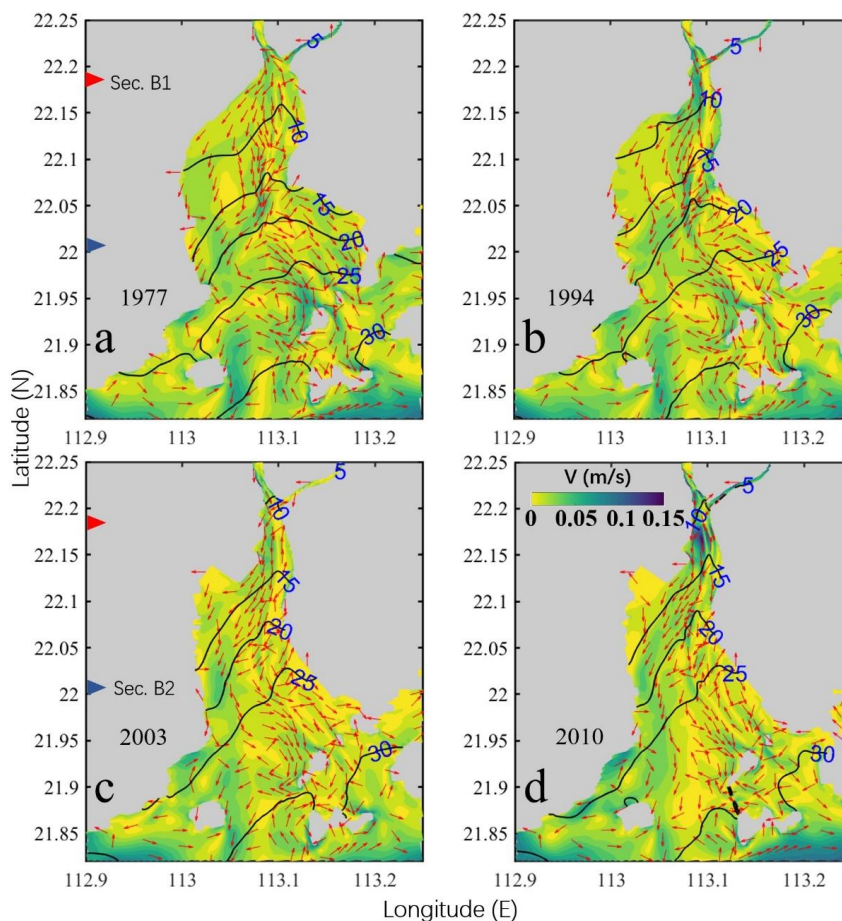
355 Here we present the changes in the tidally and vertically averaged flow and salinity  
356 during neap tides in different years in Fig. 3. In 1977 (Fig. 3a), the current speed was  
357 generally small, except at the inter-island sections and in the channel. The vertically  
358 averaged flow was seaward in the upper bay and the right part of the lower bay (looking



359 landward). It became landward at the left part of the lower bay. The 10 psu isohaline  
360 intruded into the upper bay at a latitude of 22.1 to 22.15°N. In 1994 (Fig. 3b), the current  
361 speed was increased in the channel, particularly near Sec.B1. The overall flow pattern  
362 was almost similar to that in 1977. The salt intrusion was increased, as the 10 psu  
363 isohaline intruded to a latitude of 22.15°N. In 2003 (Fig. 3c), the flow pattern still kept  
364 unchanged when compared to that in previous periods. The current speed was decreased  
365 relative to that in 1994. However, the salt intrusion became aggravated as the 10 psu  
366 isohaline had reached the bayhead at the Yamen Outlet. In 2010 (Fig. 3d), the seaward  
367 flow became more dominant in the upper bay, and more biased southwestward. The  
368 seaward flow in the channel was greater than in 2003. The salt intrusion was more  
369 serious than in 2003, as the 10 psu isohaline reached beyond the bayhead and entered  
370 into the tidal river of the estuary.

371 Overall, we observed that the tidally and vertically averaged flow during neap tides  
372 experienced an increase-decrease-increase by the topographic changes, whereas the  
373 saltwater consistently intruded further into the estuary.

374 As a supplement, we present the horizontal distributions of tidally averaged  
375 surface and bottom circulation and salinity during neap tides for different years in the  
376 appendix (Figs. A. 5 and 6). Over the study period, the enhancement of salt intrusion  
377 was stronger for the bottom layer and weaker for the surface layer, whereas the increase  
378 in residual flow was stronger in the surface layer and weaker in the bottom layer.



379

380 Fig. 3. Patterns of the vertical-averaged horizontal circulation during neap tide in 1977(a1),  
381 1994(a2), 2003(a3), and 2004(a4). The magnitude of the current is represented by the color  
382 shading, while the current direction is shown by the arrows. The salinity is depicted by the  
383 contour lines. The red and blue triangles depict the positions of two cross-sections (Sec.B1 and  
384 Sec.B2).

385

### 386 3.3 Changes in the estuarine circulation

387

388 Figures 4 a-d present the longitudinal estuarine circulation and the distributions of  
389 salinity isolines during the neap tide in the longitudinal section (Sec. A in Fig. 1b) in  
390 different years. The results show that the upper part of the estuary (upstream of the null

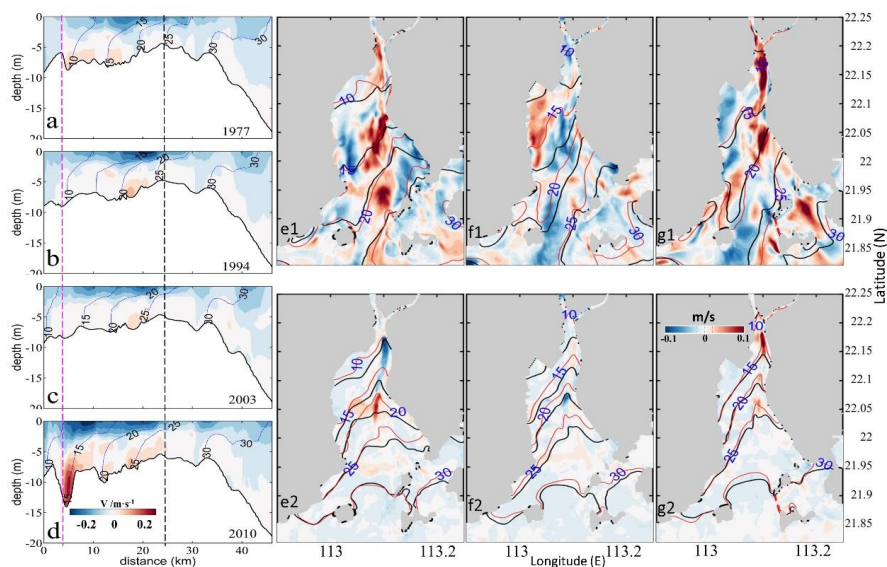




391 point) was highly stratified, and the lower part of the estuary (downstream of the null  
392 point) was well mixed. The classical exchange flow structure of “a landward residual  
393 flow near the bottom and a seaward residual flow near the surface” was more distinct  
394 upstream of the null point. Over time, the surface seaward flow became stronger and  
395 more concentrated with the narrowing of the estuary, particularly in 2010. It extended  
396 more downstream to near the estuary mouth with the narrowing of the estuary, as  
397 evidenced by the extent of the seaward flow of 0.2 m/s. Concomitantly, the bottom  
398 landward flow was strengthened and concentrated with the increase in depth.

399 We also present the changes in the surface and bottom current horizontally. Figs.  
400 4e1-g1 show that when the estuary deepened (1977-1994 and 2003-2010), the surface  
401 current speed increased in the channel, and when the estuary shoaled (1994-2003), the  
402 surface current in the channel decreased. The changes in the bottom current showed a  
403 similar trend (Figs. 4e2-g2), except at the upper part of the channel from 1977 to 1994,  
404 in which the width was considerably narrowed.

405 Along with the change in the longitudinal estuarine circulation, the salt intrusion  
406 at Sec. A did not change significantly from 1977 to 1994, but increased from 2003 on,  
407 particularly in 2010, when the isohaline of 15 psu reached Sec.B1, whose salinities  
408 were less than 12 psu in previous years (Figs. 4a-d). The salt intrusions at the surface  
409 and bottom gradually increased with the estuary narrowing (Figs. 4e1-g2).



410  
411 Fig. 4. The patterns of the estuarine circulation during the neap tide in March 1977(a), 1994(b),  
412 2003(c), and 2010(d). The thin lines are the isolines of salinity in a-d. The pink and black dotted  
413 lines represent the locations of Secs. B1 and B2, respectively. The starting point of the X-axis  
414 is Point A in Fig. 1b. Surface current differences from 1977 to 1994(e1), from 1994 to 2003(f1),  
415 and from 2003 to 2010(g1); Bottom current differences from 1977 to 1994(e2), from 1994 to  
416 2003(f2), and from 2003 to 2010(g2). The red and black lines represent the isolines of salinity  
417 in the later year and the earlier year.

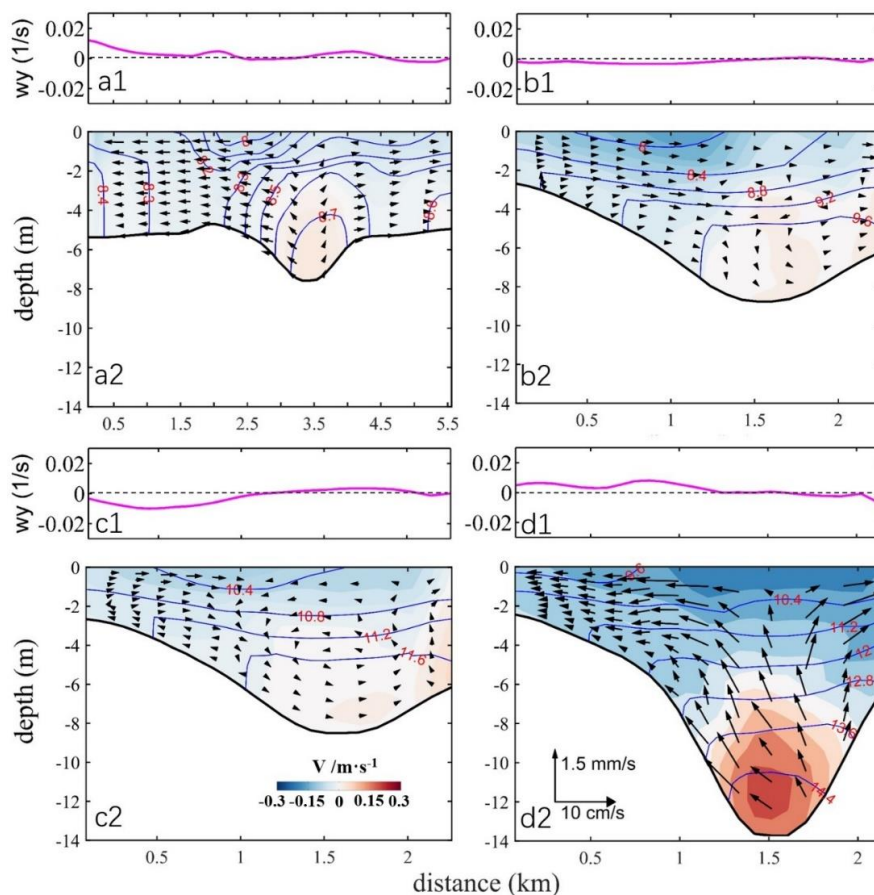
418

419 To analyze the changes of lateral circulation in the estuary, we show the structure  
420 and intensity of the lateral circulation at the two cross-sections (Figs. 5 and 6).

421 At Sec. B1 (Fig. 5), with the increase of water depth, the salinity difference  
422 between the surface and bottom increased, along with an increase in the bottom salinity,  
423 which is more than 14 psu in 2010. For the lateral circulation, there was no distinct gyre  
424 structure in 1977, but a pair of opposite vortices started to develop at the position of  
425 3.5km. In 1994, the lateral flow was dominated by an eastward flow. In 2003, a  
426 clockwise vortex was developed over the West Shoal (0.5-1 km). Meanwhile, an  
427 anticlockwise circulation with smaller vortex intensity was developed in the region of  
428 1-2km. Another clockwise circulation was developed over the East Shoal. When the



429 estuary deepened in 2010, the distribution of the lateral circulation was similar to that  
430 in 1977, but the vortex intensity increased significantly to about 2-4 times that of 1977.

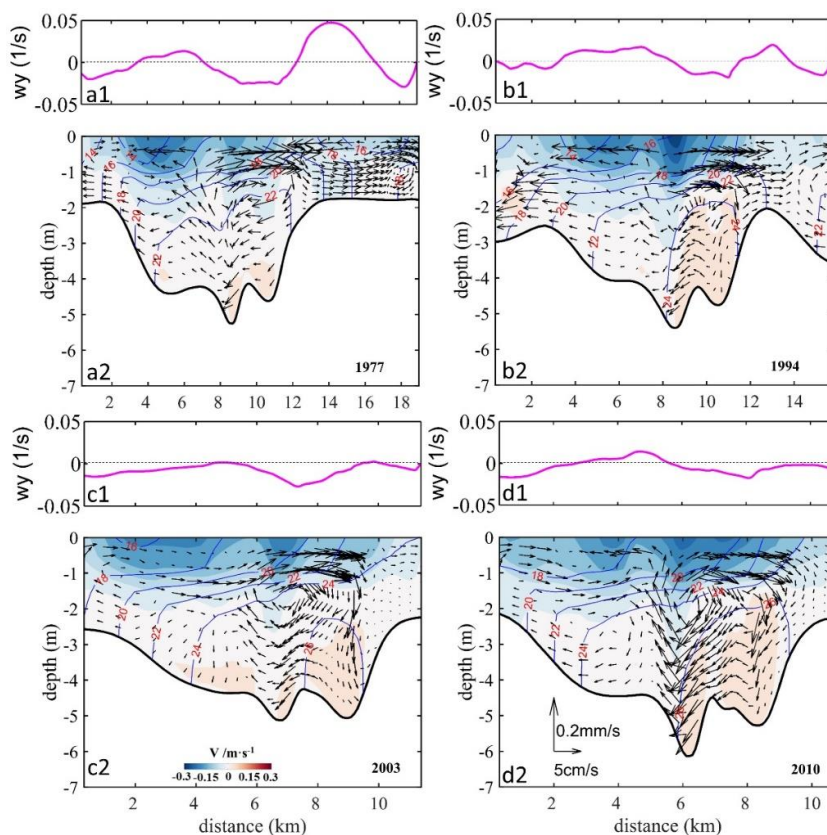


431  
432 Fig. 5. The lateral circulation and isohalines (blue lines) at Sec. B1 in 1977(a2), 1994(b2),  
433 2003(c2), and 2010(d2). The starting point of the X-axis is Point C in Fig. 2d.  $w_y$  is the  
434 longitudinal vorticity at Sec. B1 in 1977(a1), 1994(a2), 2003(a3), and 2010(a4).  
435

436 Figure 6 shows the changes in lateral circulation at Sec. B2. With the decrease of  
437 estuary width, the salinity increased in the cross-section over the years. There  
438 developed a clockwise circulation at the right of the deep channel in 1977 and 1994.  
439 This clockwise vortex was seen to move westward from 2003 on. The spatial extent of  
440 the clockwise circulation in the deep channel increased significantly over time.  
441 Clockwise vortices developed over the East Shore from 1977 to 2010, but their intensity



442 became weaker since 2003. In 1977 and 1994, the distance between the deep channel  
 443 and the East Shore was greater than 2 km, and the accommodation space was enough  
 444 for the clockwise vortices to develop sufficiently. From 2003 on, the accommodation  
 445 space at the East Shore became limited and restricted the full development of the  
 446 clockwise vortex. Over the West Shoal, the lateral circulation pattern showed an  
 447 anticlockwise circulation in 1977 and 1994. However, since 2003, the lateral circulation  
 448 over the West Shoal began to develop a two-cell pattern, with an anticlockwise gyre at  
 449 the surface and a clockwise one near the bottom. The clockwise cell developed well in  
 450 2010.



451  
 452 Fig. 6. The distribution of lateral circulation and isohalines (blue lines) at Sec. B2 in 1977(a2),  
 453 1994(b2), 2003(c2), and 2010(d2). The starting point of the X-axis is Point E in Fig. 2d.  $w_y$   
 454 is the longitudinal vorticity at Sec. B2 in 1977(a1), 1994(a2), 2003(a3), and 2010(a4).  
 455



456 As a whole, over the study period, the longitudinal estuarine circulation continued  
457 to increase, whereas the lateral circulation experienced varying changes at different  
458 cross-sections. At the upstream cross-section (B1), when the estuary narrowed, the  
459 original pattern of two-cell vortices with opposite polarity was disrupted. However, it  
460 was amplified in 2010 when the water depth was increased. At the cross-section in the  
461 middle of the estuary (B2), a similar two-cell pattern was developed. However, in 2003  
462 and 2010, the single cell at the West Shoal was split into two cells: an anticlockwise  
463 cell at the surface and a clockwise cell at the lower part.

464

### 465 **3.4 Relationship between the Changes in the intensity of estuarine circulation** 466 **and the changes in topography**

467

468 To further quantitatively identify the influence of topographic changes on the  
469 estuarine circulation, we calculated the changes in the intensity of estuarine circulations  
470 in the longitudinal and lateral directions. The magnitude of estuarine circulation in the  
471 longitudinal section was used to represent the intensity of the longitudinal estuarine  
472 circulation (Chen and Sanford, 2009). The method was to subtract the subtidal  
473 longitudinal velocity of the bottom layer from that on the surface layer. The magnitude  
474 of the vorticity in the cross-sections was used to represent the intensity of the lateral  
475 circulation (Becherer et al. 2015), and is expressed as:

$$476 \quad w_y = \partial w / \partial x - \partial u / \partial z \quad (2)$$

477 where,  $w_y$  is the longitudinal vorticity in the cross-sections.  $w$  and  $u$  are the  
478 currents in the vertical and lateral directions, respectively.  $\partial w / \partial x$  is much smaller  
479 and can be ignored, therefore, the formula for calculating the intensity of lateral  
480 circulation can be simplified as:

$$481 \quad w_y = -\partial u / \partial z \quad (3)$$

482 when  $w_y$  is positive, the lateral circulation is an anticlockwise vortex, conversely,  
483 when  $w_y$  is negative, the lateral circulation is a clockwise vortex.



484 The results of the averaged intensity of estuarine circulation along the longitudinal  
 485 section and the averaged intensity of vorticity at the cross-sections are listed in Table  
 486 4.

487  
 488 Table 4. The changes of width and depth (the maximum depth), area (cross-section area), w-to-  
 489 d, narrowing rate, deepening rate, and the intensity of circulations (w-to-d: width-to-depth ratio;  
 490 narrowing rate: the ratio of the difference of cross-section widths between two years divided  
 491 by the width in the earlier year; deepening rate: the ratio of the difference of water depth in the  
 492 cross-section between the corresponding two years divided by the earlier depth. The positive  
 493 narrowing rate indicates that the estuary is narrowed; the positive deepening rate indicates that  
 494 the estuary is deepened.)

495

		time	1977/03	1994/03	2003/03	2010/03
Sec.B1	width (km)		5.56	2.25	2.26	2.14
	depth (m)		7.58	8.76	8.50	13.73
	w-to-d		734	257	266	156
	area (km <sup>2</sup> )		0.0468	0.0213	0.0207	0.0256
	narrowing rate		\	59.50%	-0.44%	5.30%
	deepening rate		\	15.58%	-2.95%	61.47%
Sec.B2	width (km)		18.97	15.77	11.40	10.76
	depth (m)		5.25	5.40	5.12	6.13
	w-to-d		3610	2920	2230	1760
	area (km <sup>2</sup> )		0.0849	0.303	0.0647	0.0646
	narrowing rate		\	16.87%	27.71%	5.61%
	deepening rate		\	2.86%	-5.19%	19.73%
circulation intensity	longitudinal	Sec. A	0.0274	0.0428	0.0483	0.0594
	lateral	Sec. B1	0.0111	0.0146	0.0130	0.0278
		Sec. B2	0.0493	0.0460	0.0465	0.0425

496

497 Table 4 indicates that the longitudinal estuarine circulation intensity increased with  
 498 the estuary narrowing, and reached largest in 2010, which was 0.0594 m/s.

499 The lateral circulation intensity varied in different cross-sections. For Sec.B1, it  
 500 increased gradually when the estuary deepened (from 1994 to 2010). When the  
 501 deepening rate reached the maximum (61.47%) in 2010, the lateral circulation intensity  
 502 reached the maximum as well. The intensity of lateral circulation increased when the  
 503 estuary deepened and narrowed (from 1977 to 1994, and from 2003 to 2010), but it  
 504 decreased when the estuary shallowed and narrowed (from 1994 to 2003). For Sec.B2,



505 the intensity of lateral circulation decreased when the estuary deepened and narrowed  
 506 (from 1977 to 1994, and from 2003 to 2010). However, this trend was altered when the  
 507 estuary entered into the “narrowing and shallowing period”, with the deepening rate  
 508 being -5.19%. The lateral circulation intensity increased in 2003. The change in the  
 509 lateral circulation intensity indicates that changes in water depth were the dominant  
 510 factor affecting lateral circulation intensity.

511 In general, the relationship between the longitudinal estuarine circulation intensity  
 512 and the estuary width showed a monotonic decrease, while that between the  
 513 longitudinal estuarine circulation intensity and the water depth is a monotonic increase,  
 514 but the lateral circulation intensity seemed to have no simple linear relationship with  
 515 the topographic change, including changes in the estuary width, water depth, and cross-  
 516 section area.

## 518 4. Discussion

### 520 4.1 Contribution of momentum terms to the variation of the longitudinal 521 estuarine circulation

522  
 523 To explain the change in the longitudinal estuarine circulation intensity, we  
 524 conducted a diagnostic study by examining the changes in terms of the momentum  
 525 balance equations. We calculated each term of the momentum equation in the  
 526 longitudinal direction in the tidally averaged timescale:

$$527 \quad \underbrace{\frac{\partial v}{\partial t}}_{\text{local acceleration}} = \underbrace{fu}_{\text{coriolis}} - \underbrace{g \frac{\partial \eta}{\partial y}}_{\text{barotropic pressure}} - \underbrace{\frac{gz}{\rho_0} \frac{\partial \rho}{\partial y}}_{\text{baroclinic pressure}} - \underbrace{\left( u \frac{\partial v}{\partial x} + v \frac{\partial v}{\partial y} + w \frac{\partial v}{\partial z} \right)}_{\text{advection}} + \underbrace{\frac{\partial}{\partial z} \left( A_v \frac{\partial v}{\partial z} \right)}_{\text{vertical friction}}, \quad (4)$$

528 By comparing the changes in each term and linking them with the characteristics  
 529 of morphological evolution, we try to explain the response of the longitudinal estuarine  
 530 circulation to bathymetric change in the perspective of momentum balance. Though the  
 531 change in an individual momentum term in Eq. 4 can not represent the change in the  
 532 longitudinal estuarine circulation as a whole, it can reflect the change in the  
 533 corresponding component for the estuarine circulation (Cheng, 2013). For example, an



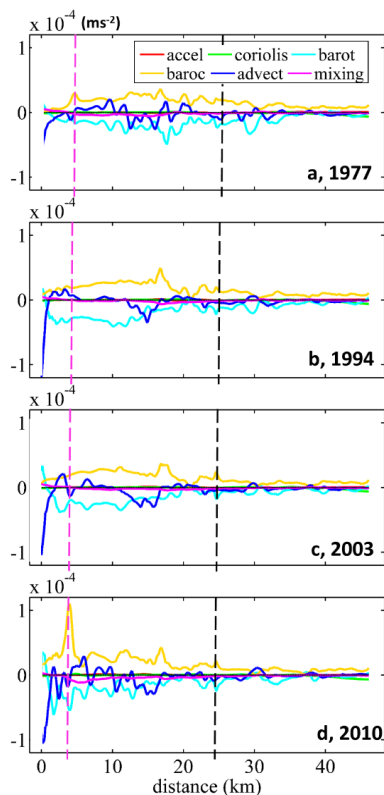
534 increase or decrease in the baroclinic pressure gradient force can reflect the change in  
535 the gravitational circulation, and the change in the advection term is representative of  
536 the change in tidal rectification. In the following, we present both the vertically  
537 averaged and depth-dependent values for these different terms along the longitudinal  
538 section in different years. It should be noted that the friction term consists of a  
539 component of the tidally mean eddy viscosity multiplied by the tidally mean vertical  
540 current shear, and a component of the correlation between eddy viscosity and vertical  
541 current shear, which is referred to as the tidal straining (Simpson et al., 1990).

542 Figure 7 shows that during the neap tide, the baroclinic pressure gradient force  
543 was balanced by barotropic gradient force, friction, and advection term in each year.  
544 This is different from the classic estuarine momentum balance (Pritchard, 1956) but  
545 consistent with the recent understanding of estuarine physics (Geyer and MacCready,  
546 2014). The Coriolis force is quite small as both the latitude of the HE and the residual  
547 current are small. The high value of the baroclinic term was observed to shift upstream  
548 over time. As the baroclinic term is the multiplication of the salinity gradient and water  
549 depth, the changes in this term over years can be induced by the change in water depth  
550 and/or the salinity gradient. It can be seen from Fig. 4 that in the north of the null point,  
551 the salt intrusion gradually moved towards the bayhead with the estuary narrowing,  
552 thus increasing the salinity gradient there. In the meantime, the upstream water depth  
553 was increased due to channel dredging, particularly in 2010. Therefore, the increase of  
554 the baroclinic force term was caused by both the increases in water depth and salinity  
555 gradient. Although the barotropic term contributed a lot to the momentum balance, it  
556 did not change obviously with the morphological evolution. The advection term at the  
557 upstream section (B1) increased slightly with the estuary narrowing, especially in the  
558 deepening part of the channel in 2010. The friction term at the upstream section (B1)  
559 was the largest in 2010, because the salt intrusion increased the vertical shear of the  
560 longitudinal current there. Nevertheless, the increase in friction term was much smaller  
561 than that of the baroclinic term. Chant et al. (2018) attributed the increase in exchange  
562 flow to the increase in horizontal salinity gradient and/or a reduction in vertical mixing





563 by deepening, but in our case, the increase in baroclinic term was dominant and the  
564 change in vertical mixing even posed a reversed effect.

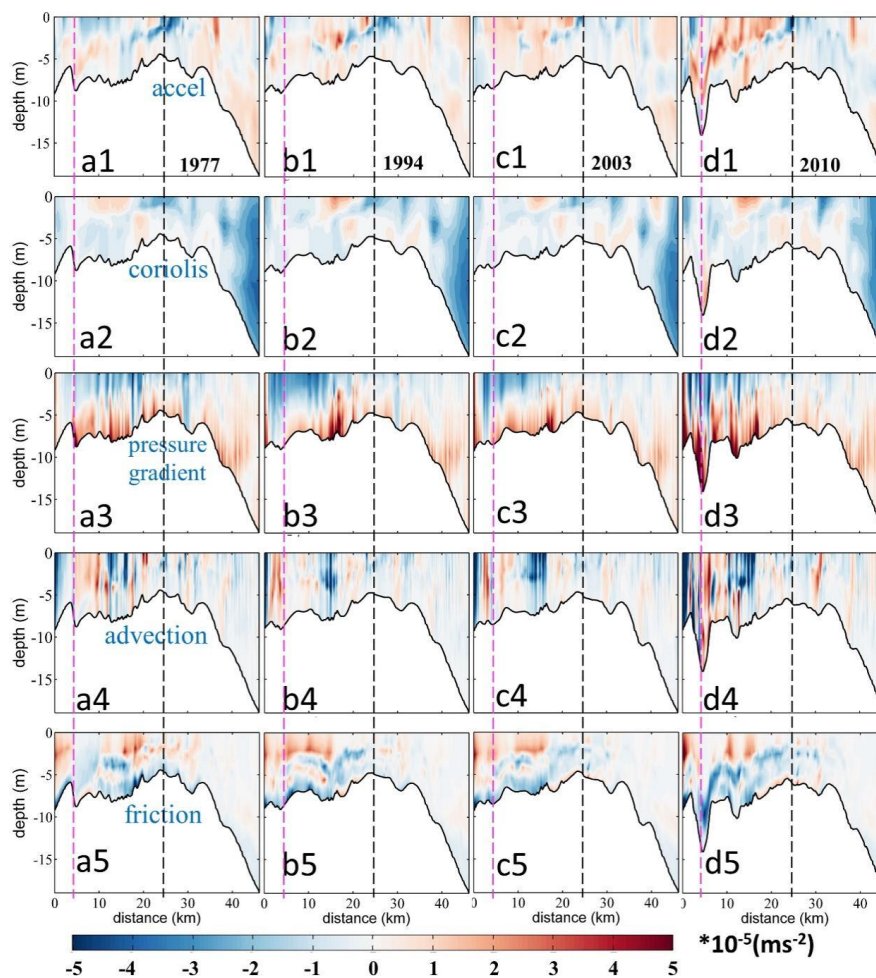


565  
566 Fig. 7. Patterns of the longitudinal momentum terms during neap tide at Sec. A in 1977(a),  
567 1994(b), 2003(c), and 2010(d). The starting point of the X-axis is Point A in Fig. 1b. “accel” in  
568 legend: local acceleration term; “barot” in legend: the barotropic gradient force term; “baroc”  
569 in legend: the baroclinic gradient force.

570  
571 In Fig.8, we present the distribution of each momentum term in the longitudinal  
572 section and its change with the morphological evolution. Among them, the distribution  
573 patterns in 1994 and 2003 were very similar. The area of maximum bottom landward  
574 pressure gradient force was shifted to the upper bay. The magnitudes of the bottom  
575 pressure gradient force in 1994 and 2003 were greater than that in 1977, but less than  
576 that in 2010. The advection term alternated between positive and negative along Sec.  
577 A, and was increased in the upper part of Sec. A in 2010. The friction term generally



578 shows a pattern of positive in the upper part and negative in the lower part of the water  
579 column, opposite to the estuarine circulation. In the region where the seaward flow was  
580 dominant in the whole water column (around 30 km), the friction was positive near the  
581 bottom. It can be seen that near Sec. B1, the friction at the bottom increased in 2010,  
582 showing an increase in the bottom landward flow.

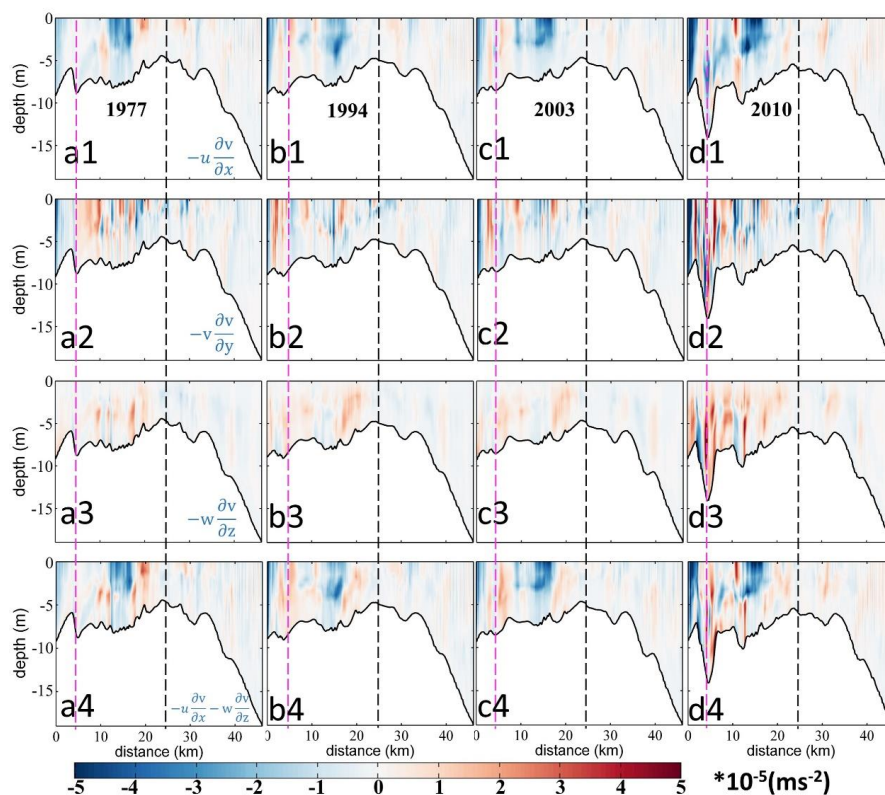


583  
584 Fig. 8. Patterns of the longitudinal momentum terms during neap tide at Sec. A. (a1-d1): The  
585 local acceleration term. (a2-d2): The Coriolis term. (a3-d3): The pressure gradient force term.  
586 (a4-d4): The advection term. (a5-d5): The friction (vertical mixing term). 1977, 1994, 2003,  
587 and 2010 cases are in the first, second, third, and fourth columns, respectively. The pink and  
588 black dotted lines represent the location of Sec.B1 and Sec.B2, respectively. The starting point



589 of the X-axis is Point A in Fig. 1b. For viewing purposes, the acceleration term is multiplied by  
 590 10.

591 To further identify the changes in different terms, the advection term was divided  
 592 into lateral (X-direction), longitudinal (Y-direction), and vertical (Z-direction)  
 593 advection terms (Fig. 9). The sum of the advection terms in X and Z directions  
 594 represents the effect of the lateral circulation. The lateral and longitudinal advection  
 595 terms are collectively referred to as the horizontal advection term.



596  
 597 Fig. 9. Patterns of the longitudinal momentum terms during neap tide at Sec. A. (a1-d1): The  
 598 advection in the X direction,  $-u \frac{\partial v}{\partial x}$ . (a2-d2): The advection in the Y direction,  $-v \frac{\partial v}{\partial y}$ . (a3-d3):  
 599 The advection in the Z direction,  $-w \frac{\partial v}{\partial z}$ . (a4-d4): The sum of the advection terms in X and Z  
 600 directions. 1977, 1994, 2003, and 2010 cases are in the first, second, third, and fourth columns,  
 601 respectively. The pink and black dotted lines represent the location of Sec.B1 and Sec.B2,  
 602 respectively. The starting point of the X-axis is Point A in Fig. 1b.  
 603



604 From Fig. 9, in 2010, the advection terms in all directions increased significantly.  
605 Generally, the lateral and vertical advection competes against each other, and their  
606 additive effect is to generate a circulation similar to the gravitational circulation. This  
607 effect was the strongest in 2010 (Figs. 9a4-d4). The longitudinal advection increased in  
608 the upper part of the channel in 2010 (Figs. 9a2-d2), following the deepening and  
609 narrowing of the estuary. In the middle of the longitudinal section, it induced a seaward  
610 flow at the surface and a landward flow at the bottom, whereas at the upper part, it  
611 generates a uniformly landward flow.

612 Therefore, the maximum longitudinal estuarine circulation in 2010 was caused by  
613 the increase in the pressure gradient force and the advection term, especially the  
614 baroclinic pressure gradient force. The largest variation of the advection and pressure  
615 gradient terms occurred in the period of topography narrowing and deepening.

616 Overall, from 1977 to 2010, the baroclinic force, the friction, and the advection  
617 terms were seen to increase along the Sec. A. We will further discuss the effects of  
618 these changes on estuarine circulation.

619

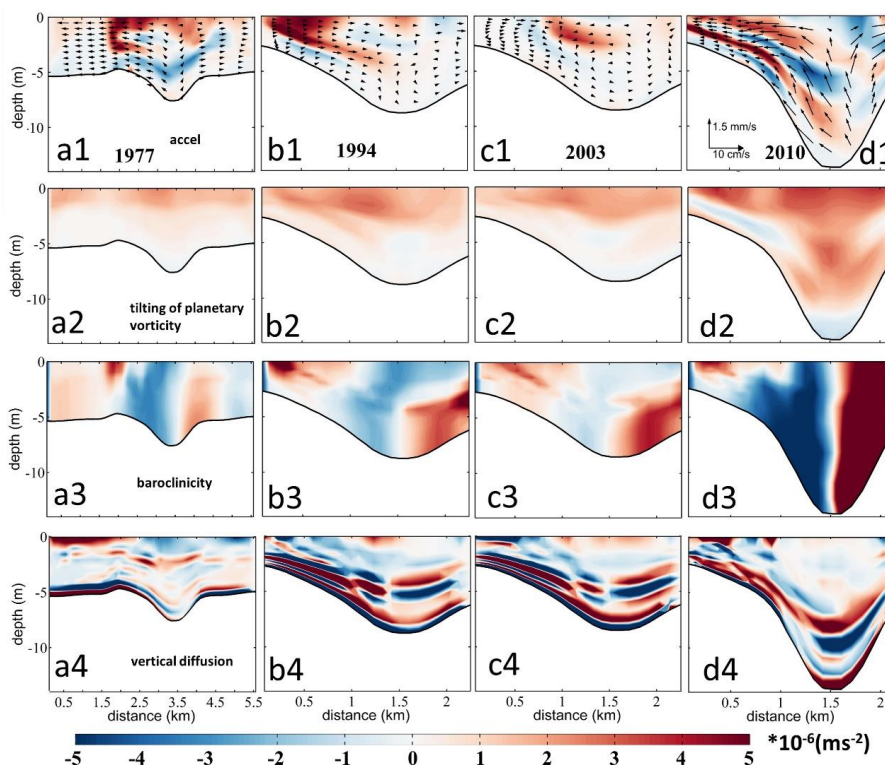
#### 620 **4.2 Analysis of the streamwise vorticity balance for the lateral flow**

621

622 In order to reveal the contribution of the vertical shear of the along-channel flow,  
623 the lateral salinity gradient, and the vertical diffusion to changes in the lateral  
624 circulation, we examine the changes in terms of the streamwise vorticity transport  
625 equation (Li et al., 2014):

$$626 \quad \frac{dw_y}{dt} = \underbrace{-f \frac{\partial v}{\partial z}}_{\text{tilting of planetary vorticity}} \underbrace{-g\beta \frac{\partial S}{\partial x}}_{\text{baroclinicity}} + \underbrace{\frac{\partial^2}{\partial z^2}(K_V w_y)}_{\text{vertical diffusion}} + \underbrace{\frac{\partial^2}{\partial x^2}(K_H w_y)}_{\text{horizontal diffusion}}, \quad (5)$$

627 In the right side of Eq. 5, the first term represents the tilting of the planetary  
628 vorticity by vertical shear in the along-channel flow, the second term is the baroclinicity  
629 caused by the lateral salinity gradient, the third is the vertical diffusion, and the fourth  
630 is the horizontal diffusion, which is typically two orders of magnitude smaller than the  
631 vertical diffusion term. Therefore, we only show the first four terms in Fig. 10.



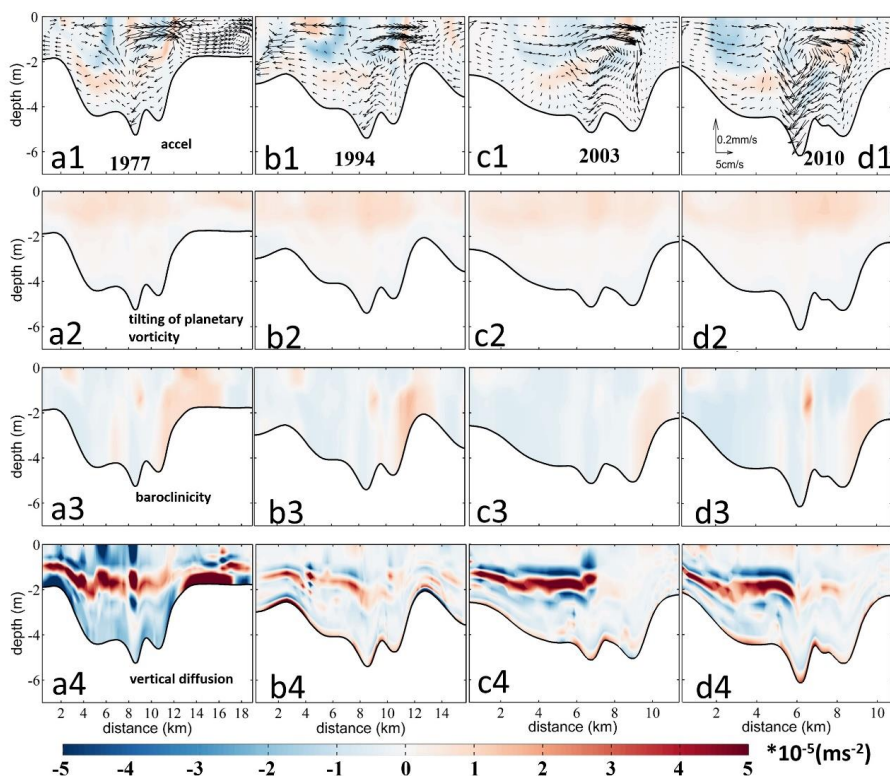
632

633 Fig. 10. Patterns of the streamwise vorticity equation terms during neap tide at Sec. B1. (a1-  
634 d1): The local acceleration term. (a2-d2): The tilting of planetary vorticity term. (a3-d3): The  
635 baroclinicity term. (a4-d4): The vertical diffusion term. The cases in 1977, 1994, 2003, and  
636 2010 are in the first, second, third, and fourth columns, respectively. The starting point of the  
637 X-axis is Point C in Fig. 2d. For viewing purposes, the acceleration term is multiplied by 5. The  
638 block arrows in a1-d1 represent the distribution of lateral circulation.  
639

640 Figure 10 shows that the changes of baroclinicity terms caused by the water depth  
641 change dominated the changes in the lateral circulation at Sec. B1. The baroclinicity  
642 term in the deep channel was generally negative at the left side of the channel, and it  
643 increased significantly in 2010, about 2-3 times the value in 1977. The baroclinicity  
644 term with positive values occurred over the West Shoal over the study period, but the  
645 areal extent occupied by the positive values decreased gradually, with its magnitude  
646 increased obviously in 1994 when the narrowing rate was the largest. A negative  
647 baroclinicity term appeared at the bottom of the West Shoal, indicating that the changes



648 in water depth can lead to changes in the pattern and magnitude of the baroclinicity  
 649 term, which was mainly caused by the changes in the salt intrusion. The tilting of the  
 650 planetary vorticity term increased with the estuary narrowing, but the increase of this  
 651 term in 2010 was greater, which was mostly caused by the depth change. The pattern  
 652 of the vertical diffusion term changed significantly in 1977 and 1994. It changed at the  
 653 surface and the bottom layers of the West Shoal: When the width decreased to about  
 654 2.5 km, the distribution of vertical diffusion was reversed compared with 1977,  
 655 indicating that it was the changes in width that altered the vertical diffusion term.



656  
 657 Fig. 11. Patterns of the streamwise vorticity equation terms during neap tide at Sec. B2. (a1-  
 658 d1): The local acceleration term. (a2-d2): The tilting of planetary vorticity term. (a3-d3): The  
 659 baroclinicity term. (a4-d4): The vertical diffusion term. The cases in 1977, 1994, 2003, and  
 660 2010 are in the first, second, third, and fourth columns, respectively. The starting point of the  
 661 X-axis is Point E in Fig. 2d. For viewing purposes, the acceleration term is multiplied by 5. The  
 662 block arrows in a1-d1 represent the distribution of lateral circulation.



663 From Fig. 11, the change in the tilting of the planetary vorticity at Sec. B2 was  
664 analogous to that at Sec. B1. The baroclinicity term did not change much, because the  
665 changes in water depth were smaller than that at Sec. B1. The clockwise circulation  
666 over the West shoal increased as the estuary deepened in 2010, because the baroclinicity  
667 term was larger with the increase of salt intrusion and vertical salinity gradient near Sec.  
668 B2. The vertical diffusion of the vorticity was overall negative, indicating its effect in  
669 dissipating the vorticity. The vertical diffusion term was larger than the baroclinicity  
670 term, especially in the middle water, which was inconsistent with the conclusion that  
671 the baroclinicity term is the most important one in the lateral circulation (Li et al., 2014).  
672 The reason may be that in our study site, the vertical mixing was strong as the estuary  
673 was shallow. However, the existence of a pycnocline greatly weakened the momentum  
674 exchange between the upper and lower layers: above the pycnocline, the tilting of the  
675 planetary vorticity was dominant; whereas, under the pycnocline, the baroclinic term  
676 was dominant. The decrease of the estuary width changed the magnitude and pattern of  
677 the vertical diffusion term, especially when the estuary width was less than 15 km, the  
678 area with a large positive value at the bottom of the East Shoal disappeared, and the  
679 magnitude of the negative value decreased greatly at the easternmost of the section. It  
680 indicates that in a shallow estuary, the vertical diffusion term caused by the width  
681 change is also important.

682 In Summary, the tilting of the planetary vorticity increased with the decrease of  
683 width or with the increase of water depth. The variation of estuary width was  
684 responsible for the changes in the vertical diffusion term, and the changes in water depth  
685 were responsible for the changes in the baroclinicity term. The increase of the  
686 longitudinal estuary circulation can increase the baroclinicity term of the cross-sections  
687 by increasing the salinity gradient near the cross-sections, which mainly occurred in the  
688 periods of the estuary deepening. The deepening rate of Sec.B1 was the highest (61%)  
689 in 2010, which led to the strongest lateral circulation in 2010. The lateral circulation  
690 intensity decreased when the estuary narrowed in 2003 due to the decreased  
691 baroclinicity term. In addition, the shallowing was the main reason for the pattern



692 change of the lateral circulation at Sec.B2. At Sec. B2, the narrowing rate was the  
693 largest in 2003, and the adjustment of vertical diffusion term resulted in an increased  
694 lateral circulation from 1994 to 2003. The decrease of the clockwise circulation at the  
695 East Shoal was mainly related to the adjustment of the vertical diffusion term to the  
696 baroclinicity term.

697

### 698 **4.3 Comparison to theoretical results and other estuaries influenced by human** 699 **interventions**

700

701 The longitudinal estuarine circulation is generated by the river discharge, Stokes  
702 return flow, longitudinal baroclinic pressure force, tidal straining, and advection (Geyer  
703 and Maccready, 2014). The HE features a microtidal tidal regime (tidal range less than  
704 1.5 m), and the component generated by the baroclinic pressure gradient, i.e., the  
705 gravitational circulation, would be a primary part of the longitudinal estuarine  
706 circulation. The convergent geometry makes it susceptible to the residual flow induced  
707 by the longitudinal advection (Burchard et al., 2014). However, as seen above, the  
708 horizontal advection also plays a role in generating the estuarine circulation.

709 With channel deepening and width narrowing in the HE, the gravitational  
710 circulation was increased by the increased baroclinic pressure gradient force. Based on  
711 Geyer (2010), the gravitational circulation in a straight estuary of rectangular cross-  
712 section is scaled as:

$$713 \quad v_g = a(\beta g s_0 h)^{1/5} U_r^{1/5} U_t^{2/5} = a(\beta g s_0 h)^{1/5} R^{1/5} (wh)^{-1/5} U_t^{2/5}, \quad (6)$$

714 in which  $a$  is a constant,  $\beta$  is the salinity expansion coefficient,  $g$  is the gravity  
715 acceleration,  $s_0$  is the oceanic salinity,  $R$  is the river discharge,  $w$  is the width of  
716 the cross-section,  $U_t$  is the tidal velocity amplitude,  $h$  is the water depth,  $U_r$  is the  
717 outflow velocity associated with the river discharge. Where  $u_r = Q_r/A_{CS}$  ( $Q_r$  is the  
718 freshwater outflow,  $A_{CS}$  being the local cross-sectional area of the estuary).





719 If we simply assume that the change in tidal current amplitude follows the Green's  
720 law  $U_t = U_0 \sqrt{\frac{w_0 h_0}{wh}}$  (here  $w_0$  and  $h_0$  is the width and depth at the estuary mouth,  
721 respectively), then the gravitational circulation becomes:

$$\begin{aligned} 722 \quad v_g &= a(\beta g s_0 h)^{1/5} R^{1/5} (wh)^{-1/5} U_0^{2/5} (w_0 h_0)^{1/5} (wh)^{-1/5} \\ 723 \quad &= a_1 (\beta g s_0 R w_0 h_0)^{1/5} U_0^{2/5} w^{-2/5} h^{-1/5}, \quad (7) \end{aligned}$$

724 It indicates that the gravitational circulation is inversely related to the water depth  
725 and width in the estuary, with a weaker dependence on the water depth. In Chant et al.  
726 (2018), the gravitational circulation is completely unrelated to the water depth in their

727 equation (2), which is  $v_g \propto \left(\frac{g'R}{w}\right)^{\frac{1}{3}}$ , in which the  $g'$  is the reduced gravity acceleration.

728 This seems to contradict the situations occurring in many estuaries, such as in the Coos  
729 Bay (Eidam et al., 2020), Tampa Bay (Zhu et al., 2015), Changjiang Estuary (Zhu,  
730 2018), Ems estuary (Van Maren et al., 2015), Hudson Estuary (Ralston and Geyer,  
731 2019), and Newark Bay of the Delaware estuary (Chant et al., 2018). In all these  
732 estuaries, the gravitational circulation demonstrated an increase with the deepening of  
733 the channel. It suggests that the changes in gravitational circulation vary in different  
734 parts of the estuary and the longitudinal salinity gradient may not catch up with the  
735 change in water depth in the analytical solution, proposed by Chant et al. (2018) and  
736 Ralston and Geyer (2019). In our study site, the salinity gradient at the upstream part  
737 of the longitudinal section was increased owing to an enhanced salt intrusion where  
738 water depth increased, which led to an increased gravitational circulation in the  
739 upstream of the HE (Fig. 4).

740 The tidal straining-induced estuarine circulation is another important component of  
741 longitudinal estuarine circulation. The straining-induced circulation is the covariance  
742 of the eddy viscosity and the vertical shear of the longitudinal flow (ESCO) in a tidal  
743 cycle and is included in the term of internal friction. Cheng et al. (2010) have indicated  
744 that ESCO-induced flow dominates the gravitational circulation in periodically  
745 stratified estuaries with strong tides, having the same structure as the gravitational

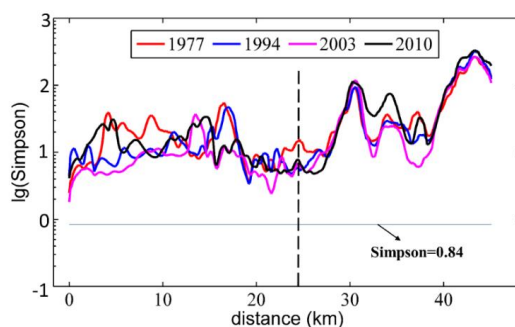


746 circulation. It has the same order of magnitude in weakly stratified estuaries with  
747 moderate tides, and is less important in highly stratified estuaries with weak tides, even  
748 with a reversed structure with the gravitational circulation. As indicated by Becherer et  
749 al. (2015), the strength of the straining-induced circulation is dependent on the Simpson  
750 number (or the horizontal Richardson number). The Simpson number is expressed as:

$$751 \quad S_i = g\beta \frac{ds}{dy} \frac{h^2}{u_*^3}, \quad (8)$$

752 in which  $u_*$  is the bottom friction velocity, represented by  $u_* = \sqrt{C_d}U_t$ , where  $C_d$  is  
753 the bottom friction coefficient and  $U_t$  is the tidal velocity amplitude.

754 When  $S_i$  lies in the range of 0.088 to 0.84, the water column stays periodically  
755 stratified, and the straining-induced circulation is an important component in the  
756 longitudinal estuarine circulation. When  $S_i$  is larger than 0.84, the water column is in  
757 a persistent stratified situation, and the straining-induced circulation becomes weaker.  
758 We calculated the  $S_i$  along the longitudinal section in different years and depict them  
759 in Fig. 12.



760  
761 Fig. 12. Distribution of the Simpson number in different years along the longitudinal section.  
762 The Y-axis represents the logarithmic of the  $S_i$ . The black dotted line represents the location  
763 of the null point.  
764

765 It indicates that along the longitudinal section, the  $S_i$  number was mostly above  
766 the criterion of 0.84, showing that the straining-induced circulation is not significant.  
767 The  $S_i$  number was the smallest in 2003 and the largest in 2010. It indicates that with  
768 the narrowing and deepening of the HE, the straining-induced circulation became



769 weaker. This is consistent with Burchard et al. (2014) and Schulz et al. (2015). It  
770 indicates that with the human interventions, the straining-induced circulation became  
771 less important in the longitudinal estuarine circulation.

772 For the advection-induced longitudinal estuarine circulation, we noted that the  
773 longitudinal and vertical advection terms were smaller than the lateral advection. Based  
774 on Cheng and Valle-Levinson (2009), the lateral advection-induced longitudinal  
775 circulation is proportional to the ratio of  $h/(wK_m)$ , where  $w$  is the width, and  $K_m$  is  
776 the eddy viscosity. It shows that in a narrower and deeper estuary, the lateral advection  
777 has a larger effect in influencing the longitudinal estuarine circulation. Lerczak and  
778 Geyer (2004) also showed that the effect of the lateral advection on longitudinal  
779 circulation is stronger for narrower estuaries. Our results show that with the narrowing  
780 and deepening of the estuary, not only the lateral advection but also the longitudinal  
781 advection has great influences on the longitudinal estuarine circulation.

782

#### 783 **4.4 The possible future development of the estuarine circulation and its** 784 **implications**

785

786 The pattern of lateral circulation during the dry season in the HE experienced a  
787 dramatic change from 2003 to 2010 in the West Shoal at Sec. B2, from an under-  
788 developed circulation structure to a complete clockwise vortex in 2010. This transition  
789 was associated with the increase in lateral salinity gradient, the increase in longitudinal  
790 bottom landward flow, and a decrease of friction by the increased water depth and  
791 stratification.

792 The mechanisms for the lateral circulation during the wet season have been  
793 revealed by Chen et al. (2020b), who showed that it was primarily driven by the  
794 barotropic process, i.e., the water elevation gradient, and thus by the intensity of the  
795 ebb jet. Different from the wet season when the river discharge was more dominant, the  
796 lateral circulation in the dry season was more affected by the baroclinic effect. We  
797 speculate that with the narrowing and deepening of the estuary, the lateral circulation



798 even in the wet season will be enhanced with the ebb jet in the deep channel  
799 strengthened.

800 In the HE, the channel underwent siltation, and sediment was carried from the  
801 channels to side banks by the lateral circulation, making the estuary overall shallower  
802 in 2003. In 2005, dredging of the channel increased the channel depth (Luo, 2010),  
803 resulting in a high deepening rate, and increased the longitudinal estuarine circulation,  
804 though the lateral circulation decreased slightly by the smaller rate of convergence. If  
805 reclamation did not occur as frequently as it did in the last century, and the channel  
806 dredging continued, the estuarine circulation of the estuary will in general keep  
807 increasing with the increase in water depth, and there exists positive feedback. However,  
808 as revealed in Eq. (6) and Eq. (2) in Chant et al. (2018), with the increase in salt  
809 intrusion, the longitudinal salinity gradient will decrease, showing negative feedback.  
810 Moreover, Schulz et al. (2015) noted that estuarine circulation exhibits a distinct  
811 maximum in medium-wide channels by comparing estuarine circulation under different  
812 width-to-depth ratios. In our study, as shown in Table 4, the width-to-depth ratio has  
813 been decreasing from 1977 to 2010, but the estuarine circulation has been increasing.  
814 The difference would be caused by the fact that in our study site, the tidal mixing is not  
815 strong enough to generate an effective tidal straining-induced circulation.

816 The changes in the estuarine circulation have important implications for sediment  
817 transport and morphological evolution in the HE. With the increase of longitudinal  
818 estuarine circulation, the sediment trapping effect is expected to be enhanced, thus more  
819 riverine sediment would be trapped inside the estuary. In the meantime, the change in  
820 lateral circulation would decrease the sediment advection from the channel to the West  
821 Shoal, which occurred in the wet season and was favorable for the siltation in the West  
822 Shoal (Chen et al., 2020b).

823 In this study, the model used was only driven by river discharge and tides, without  
824 considering the effects of winds, waves, and other upstream flows into the estuary.  
825 Future work could incorporate the above factors to improve the model's accuracy.



826

## 827 **5. Conclusion**

828

829 This study investigated the morphological evolution of the HE from 1977 to 2010  
830 using ArcGIS and remote sensing. It was noted that the West Channel of the HE  
831 disappeared, causing the morphological pattern to change from “two channels and  
832 three shoals” gradually to “one channel and two shoals” throughout the years. Due to  
833 the reclamation and development of salt marshes along the estuarine banks, the estuary  
834 has been experiencing continuous narrowing. Meanwhile, channel dredging has  
835 deepened the estuary over the study period. The intensity of the longitudinal estuarine  
836 circulation kept increasing as the estuary width continued to decrease. The trend of the  
837 lateral circulation intensity altered when the estuary shallowed (from 1994 to 2003).

838 The changes in the longitudinal estuarine circulation were dominated by the  
839 changes in the baroclinic pressure gradient force and advection. As the estuary was  
840 narrowing and deepening, the pressure gradient force and advection term (especially  
841 the horizontal advection term) increased, which increased the longitudinal circulation.  
842 The change in lateral circulation intensity was mainly caused by the change of the  
843 vertical shear of the longitudinal subtidal flow, the lateral salinity gradient, and the  
844 vertical dissipation term. The changes in water depth were the dominant factor  
845 affecting lateral circulation intensity. The increase of water depth enhanced the  
846 longitudinal circulation and the lateral circulation of the upstream cross-section in  
847 2010. The changes in the estuarine circulation have great implications for the sediment  
848 transport in the HE, which would be explored in the next step.

849

## 850 **Data availability**

851 A total of 142G data of 66 images (Table 1) covering the PRD during cloudless days  
852 in multiple years (from 1973 to 2018) were downloaded from <http://www.gscloud.cn/>.

853



854 **Author contributions**

855 RuiZhang: Writing - original draft, model runs and analyses. Bo Hong: Writing -  
856 review. Lei Zhu: Writing - review. Wenping Gong: Writing - review & editing,  
857 Conceptualization, Funding acquisition. Heng Zhang: Visualization, Funding  
858 acquisition.

859

860 **Competing interests**

861 The authors declare that they have no conflict of interest.

862

863 **Acknowledgments**

864

865 This research is funded by the National Natural Science Foundation of China [Grant  
866 nos. 51761135021, 41506102, 41890851]. We would like to thank the National  
867 Aeronautics and Space Administration (NASA) for providing the Landsat remote  
868 sensing data. We are very grateful to graduate students in our team from Sun Yat-sen  
869 for their help in fieldwork and sediment sample analysis in the indoor laboratory.

870

871

872

873

874

875

876

877

878

879

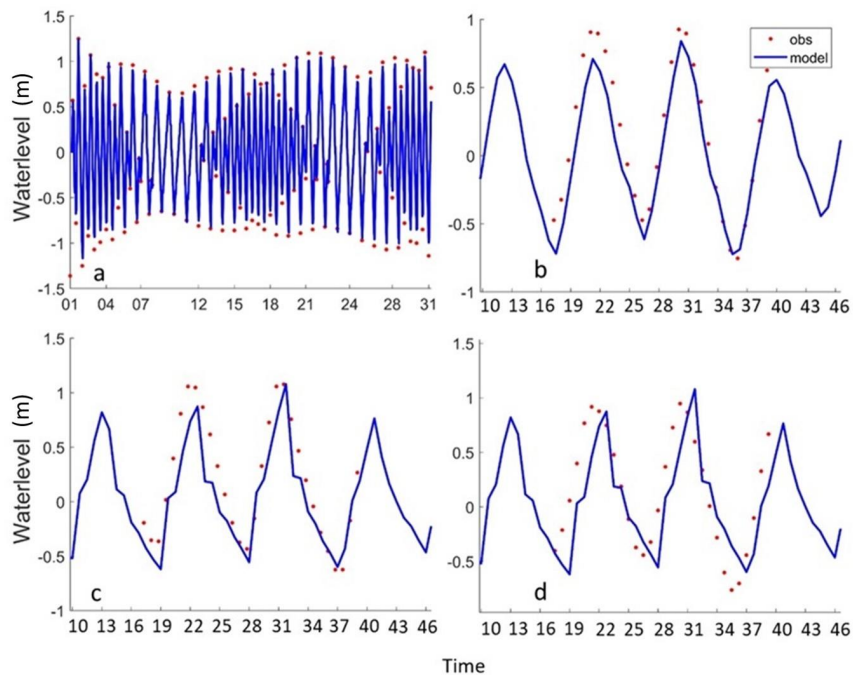
880

881

882

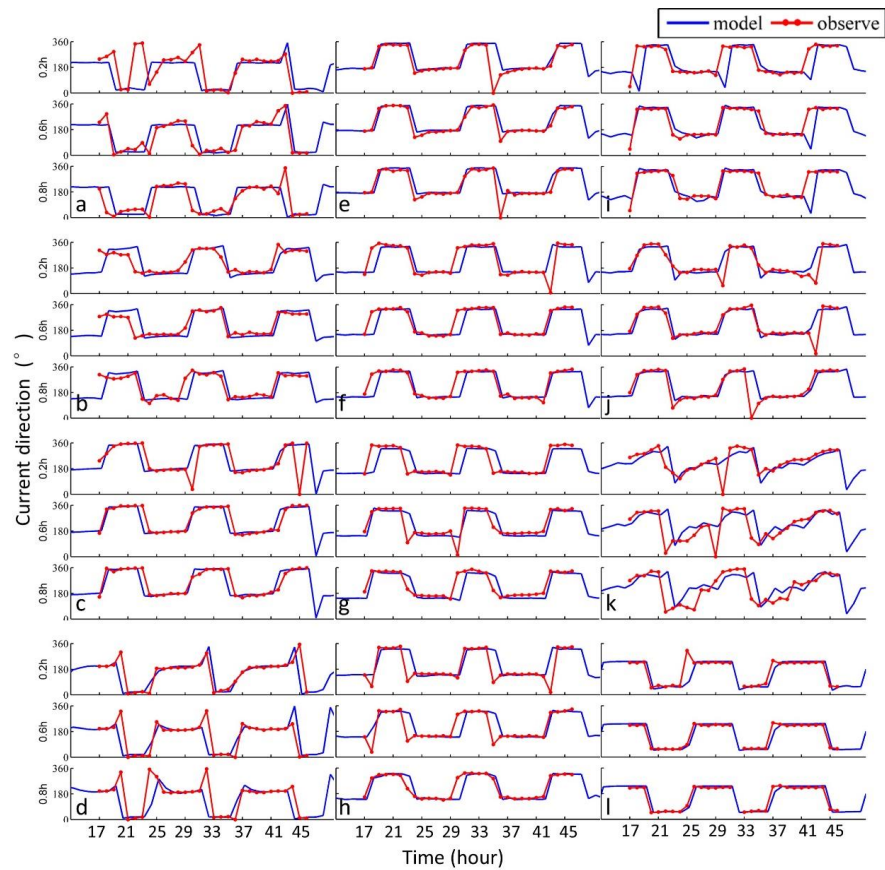


883 **Appendix A**



884  
885 Fig. A. 1. Validation of water level of the MD2 model at 4 stations (S6 (a): SK=0.9969, DJ (b):  
886 SK=0.9337, S1 (c): SK=0.8652, and GL (d): SK=0.8928) in March 2010. The red dots and blue  
887 lines represent observation and simulated results, respectively. The station locations are shown  
888 in Fig. 1b. Time in (a) is days from 2010/3/1, in (b-d) is hours from 2010/3/17 00:00.

889

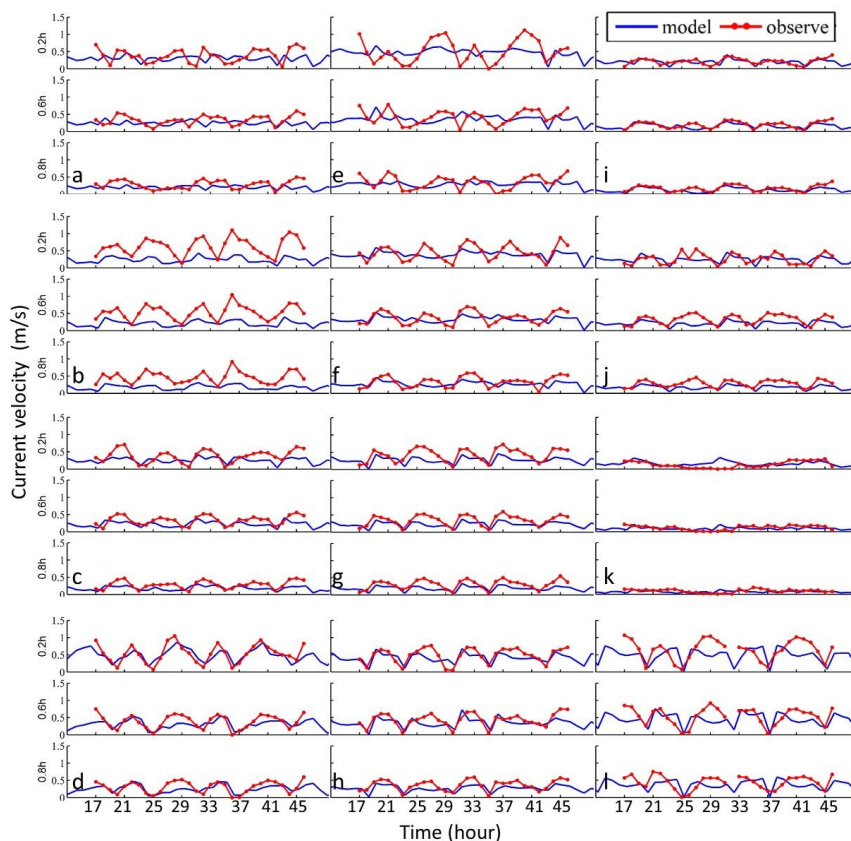


890  
891 Fig. A. 2. Validation of current direction of the MD2 model at 12 stations (DJ (a), GL (b), HB  
892 (c), S2(d), S3(e), S4(f), S5(g), S7(h), S6(i), S8(j), S9(k), and S1(l)) in March 2010. The red and  
893 blue lines represent observation and simulation results, respectively. The station locations are  
894 shown in Fig. 1b. Time is hours from 2010/3/17 00:00.

895

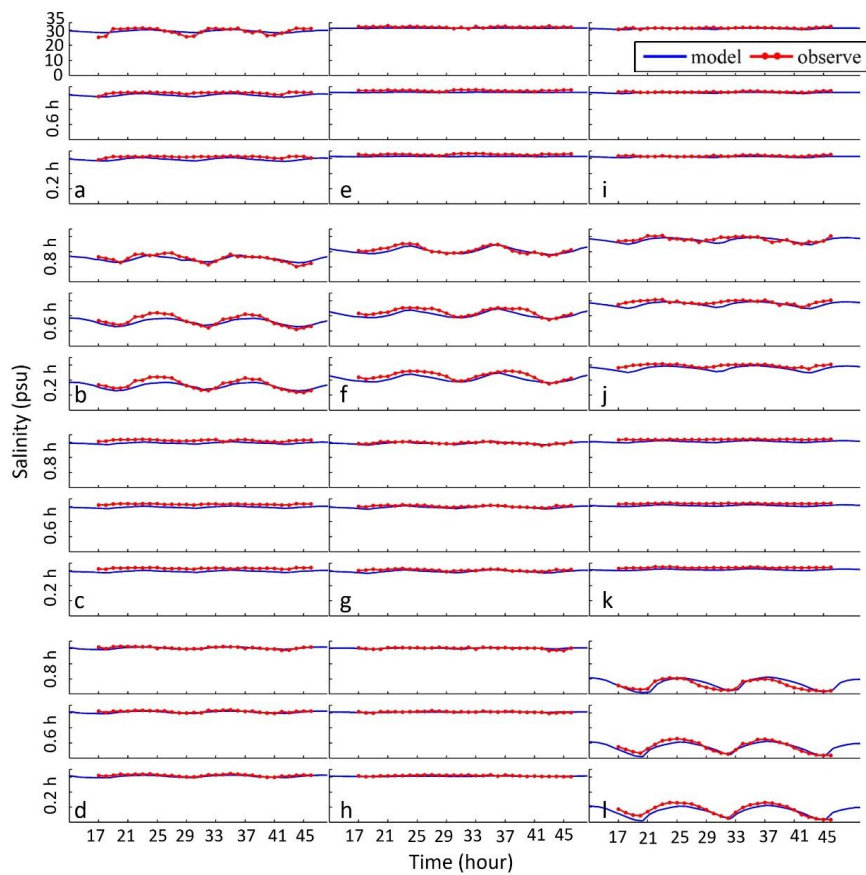
896





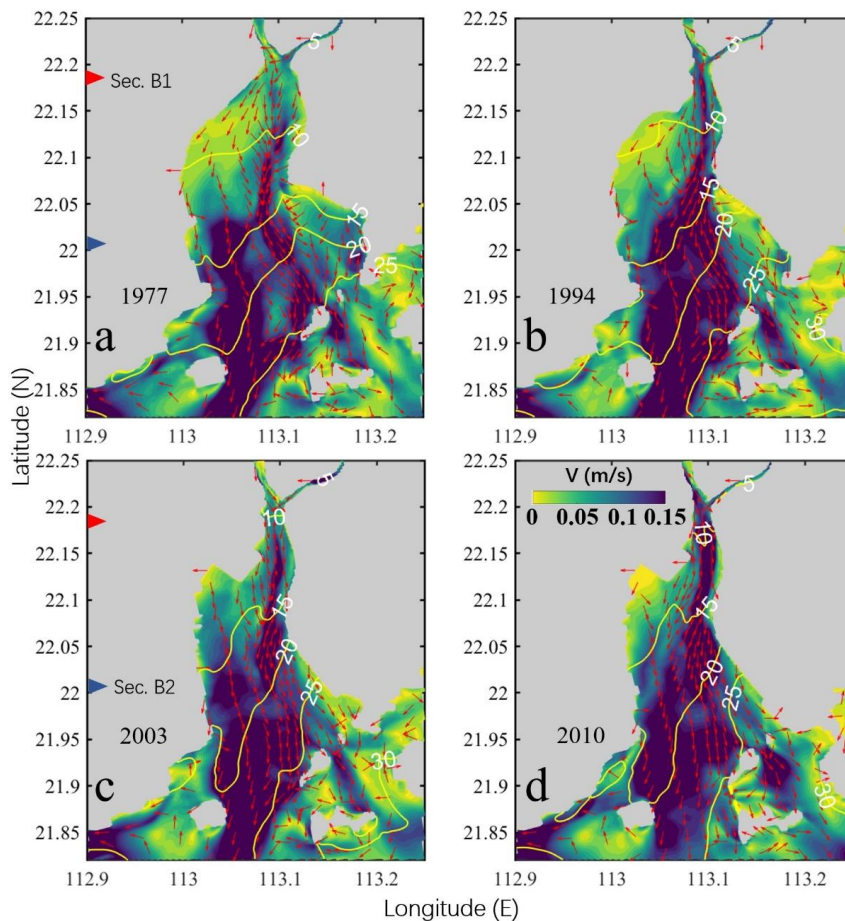
897  
898 Fig. A. 3. Validation of current velocity of the MD2 model at 12 stations (DJ (a), GL (b), HB  
899 (c), S2(d), S3(e), S4(f), S5(g), S7(h), S6(i), S8(j), S9(k), and S1(l)) in March 2010. The red and  
900 blue lines represent observed and simulated results, respectively. The station locations are  
901 shown in Fig. 1b. Time is hours from 2010/3/17 00:00.

902  
903  
904



905  
906 Fig. A. 4. Validation of salinity of the MD2 model at 12 stations (DJ (a), GL (b), HB (c), S2(d),  
907 S3(e), S4(f), S5(g), S7(h), S6(i), S8(j), S9(k), and S1(l)) in March 2010. The red and blue lines  
908 represent observed and simulated results, respectively. The station locations are shown in Fig.  
909 1b. Time is hours from 2010/3/17 00:00.

910  
911  
912  
913  
914  
915



916

917 Fig. A. 5. Patterns of the horizontal circulation at the surface during neap tide in 1977(a1),  
918 1994(a2), 2003(a3), and 2004(a4). The magnitude of the current is represented by the color  
919 shading, while the current direction is shown by the arrows. The salinity is depicted by the  
920 contour lines. The red and blue triangles depict the positions of two cross-sections (Sec.B1 and  
921 Sec.B2).

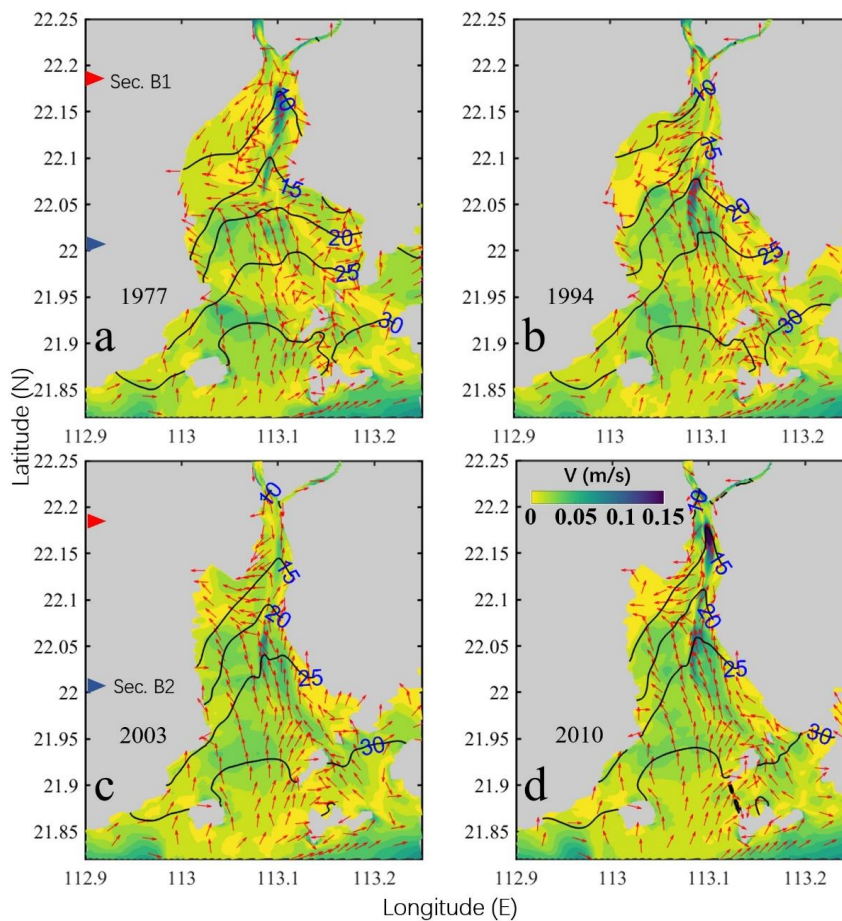
922

923

924

925

926



927

928 Fig. A. 6. Patterns of the horizontal circulation at the bottom during neap tide in 1977(a1),  
929 1994(a2), 2003(a3), and 2004(a4). The magnitude of the current is represented by the color  
930 shading, while the current direction is shown by the arrows. The salinity is depicted by the  
931 contour lines. The red and blue triangles denote the positions of two cross-sections (Sec.B1 and  
932 Sec.B2).

933

934

935

936

937

938

939

940



941 **References**

- 942
- 943 Ai, B., Zhang, R., Zhang, H., Ma, C. L. and Gu, F. G.: Dynamic process and artificial mechanism of  
944 coastline change in the Pearl River Estuary, *Regional Studies in Marine Science*, 30, 100715, 2019.
- 945 Amin, M.: On perturbations of harmonic constants in the Thames Estuary, *Geophysical Journal of the*  
946 *Royal Astronomical Society*, 73, 587-603, 1983.
- 947 Becherer, J., Stacey, M. T., Umlauf, L. and Burchard, H.: Lateral circulation generates flood tide  
948 stratification and estuarine exchange flow in a curved tidal inlet, *J. Phys. Oceanogr.*, 45, 638-656,  
949 2015.
- 950 Burchard, H., Hetland, R. D., Schulz, E. and Schuttelaars, H. M.: Drivers of Residual Estuarine  
951 Circulation in Tidally Energetic Estuaries: Straight and Irrotational Channels with Parabolic Cross  
952 Section, *J. Phys. Oceanogr.*, 41, 548-570, 2010.
- 953 Burchard, H., Schulz, E. and Schuttelaars, H. M.: Impact of estuarine convergence on residual circulation  
954 in tidally energetic estuaries and inlets, *Geophys. Res. Lett.*, 41, 913-919, 2014.
- 955 Chant, R. J., Sommerfield, C. K. and Talke, S. A.: Impact of channel deepening on tidal and gravitational  
956 circulation in a highly engineered estuarine basin, *Estuar. Coast.*, 41, 1587-1600, 2018.
- 957 Chen, L. H., Gong, W. P., Scully, M. E., Zhang, H., Cheng, W. C. and Li, W.: Axial wind effects on  
958 stratification and longitudinal sediment transport in a convergent estuary during wet season, *Journal*  
959 *of Geophysical Research: Oceans*, 125, e2019J-e15254J, 2020a.
- 960 Chen, L. H., Gong, W. P., Zhang, H., Zhu, L. and Cheng, W. C.: Lateral circulation and associated  
961 sediment transport in a convergent estuary, *Journal of Geophysical Research: Oceans*, 125, e2019J-  
962 e15926J, 2020b.
- 963 Chen, S. N. and Sanford, L. P.: Axial Wind Effects on Stratification and Longitudinal Salt Transport in  
964 an Idealized, Partially Mixed Estuary, *J. Phys. Oceanogr.*, 39, 1905-1920, 10.1175/2009JPO4016.1,  
965 2009.
- 966 Cheng, P.: Decomposition of Residual Circulation in Estuaries, *Journal of Atmospheric & Oceanic*  
967 *Technology*, 31, 698-713, 2013.
- 968 Cheng, P. and Valle-Levinson, A.: Influence of lateral advection on residual currents in microtidal  
969 estuaries, *J. Phys. Oceanogr.*, 39, 3177-3190, 2009.
- 970 Cheng, P., Valle-Levinson, A. and De Swart, H. E.: Residual currents induced by asymmetric tidal  
971 mixing in weakly stratified narrow estuaries, *J. Phys. Oceanogr.*, 40, 2135-2147, 2010.
- 972 Chernetsky, A. S., Schuttelaars, H. M. and Talke, S. A.: The Effect of Tidal Asymmetry and Temporal  
973 Settling Lag on Sediment Trapping in Tidal Estuaries, *Ocean Dynam.*, 60, 1219-1241, 2010.
- 974 Dyer, K. R. 1977. Lateral circulation effects in estuaries. *National Academy of Sciences*, p. 22-29.
- 975 Eidam, E. F., Sutherland, D. A., Ralston, D. K., Dye, B., Conroy, T., Schmitt, J., Ruggiero, P. and Wood,  
976 J.: Impacts of 150 Years of Shoreline and Bathymetric Change in the Coos Estuary, Oregon, USA,  
977 *Estuar. Coast.*, 1-19, 2020.
- 978 Fischer, H. B.: Mixing and Dispersion in Estuaries, *Annu. Rev. Fluid Mech.*, 8, 107-133,  
979 10.1146/annurev.fl.08.010176.000543, 1976.
- 980 Geyer, W. R.: Estuarine salinity structure and circulation, *Contemporary issues in estuarine physics*, 12,  
981 26, 2010.
- 982 Geyer, W. R. and Maccready, P.: The Estuarine Circulation, *Annu. Rev. Fluid Mech.*, 46, 175-197, 2014.
- 983 Gong, W. P., Jia, L. W., Shen, J. and Liu, J. T.: Sediment transport in response to changes in river



- 984 discharge and tidal mixing in a funnel-shaped micro-tidal estuary, *Cont. Shelf Res.*, 76, 89-107,  
985 2014.
- 986 Gong, W. P., Liu, H., Ren, J. and Yu, H. B.: The study of tidal propagation in the Huangmaohai estuary  
987 and its underlying mechanisms, *Acta Oceanol. Sin.*, 34, 41-54, 2012.
- 988 Gong, W. P., Schuttelaars, H. and Zhang, H.: Tidal asymmetry in a funnel-shaped estuary with mixed  
989 semidiurnal tides, *Ocean Dynam.*, 66, 637-658, 2016.
- 990 Huang, T. 2011. Study on abnormal changes of tidal range in the huangmaohai estuary. *Guangdong*  
991 *Water Resources and Hydropower*, Guangzhou, China.
- 992 Jia, L. W., Luo, J. and Ren, J.: The analysis of the evolution of a sand bar and its formation in the  
993 Huangmao Bay in the Pearl River Delta, *Acta Oceanol. Sin.*, 34, 120-127, 2012.
- 994 Kjerfve, B., Stevenson, L. H., Proehl, J. A., Chrzanowski, T. H. and Kitchens, W. M.: Estimation of  
995 material fluxes in an estuarine cross section: A critical analysis of spatial measurement density and  
996 errors I, *Limnol. Oceanogr.*, 26, 325-335, 1981.
- 997 Lacy, J. R., Stacey, M. T., Burau, J. R. and Monismith, S. G.: Interaction of lateral baroclinic forcing and  
998 turbulence in an estuary, *Journal of Geophysical Research: Oceans*, 108, 1-34,  
999 <https://doi.org/10.1029/2002JC001392>, 2003.
- 1000 Lerczak, J. A. and Rockwell Geyer, W.: Modeling the Lateral Circulation in Straight, Stratified  
1001 Estuaries\*, *J. Phys. Oceanogr.*, 34, 1410-1428, 2004.
- 1002 Lesser, G. R., Roelvink, J. V., Van Kester, J. and Stelling, G. S.: Development and validation of a three-  
1003 dimensional morphological model, *Coast. Eng.*, 51, 883-915, 2004.
- 1004 Li, C. Y. and O'Donnell, J.: Tidally driven residual circulation in shallow estuaries with lateral depth  
1005 variation, *Journal of Geophysical Research Oceans*, 102, 27915-27929, 1997.
- 1006 Li, M., Cheng, P., Chant, R. J., Valle-Levinson, A. and Arnott, K.: Analysis of vortex dynamics of lateral  
1007 circulation in a straight tidal estuary, *J. Phys. Oceanogr.*, 44, 2779-2795, 2014.
- 1008 Li, W., Shi, J. Z., Pu, X. and Hu, G. D.: Circulation within curved channel of the north passage in the  
1009 changjiang river estuary: a vorticity approach, *Oceanologia et Limnologia Sinica*, 48, 682-694, 2017.
- 1010 Li, Y. B. 2019. Numerical simulation of the formation and evolution of the geomorphic characteristics  
1011 of Huangmao Sea. Dalian University of Technology, Dalian, China.
- 1012 Luo, J. 2010. Cause Analysis of Morphological evolution of Huangmao sea Estuary in the Decade to  
1013 Century-scale. Sun Yat-sen university, Guangzhou, China.
- 1014 Pritchard, D. W.: Salinity distribution and circulation in the Chesapeake Bay estuarine system.. 1, *Mar.*  
1015 *Res.*, 11, 106-123, 1952.
- 1016 Pritchard, D. W.: The dynamic structure of a coastal plain estuary, *J Marine Res*, 15, 33-42, 1956.
- 1017 Ralston, D. K. and Geyer, W. R.: Response to channel deepening of the salinity intrusion, estuarine  
1018 circulation, and stratification in an urbanized estuary, *Journal of Geophysical Research: Oceans*,  
1019 124, 4784-4802, 2019.
- 1020 Salles, P., Valle-Levinson, A., Sottolichio, A. and Senechal, N.: Wind - driven modifications to the  
1021 residual circulation in an ebb - tidal delta: Arcachon Lagoon, Southwestern France, *Journal of*  
1022 *Geophysical Research Oceans*, 120, 728-740, 2015.
- 1023 Schulz, E., Schuttelaars, H. M., Gr We, U. and Burchard, H.: Impact of the depth-to-width ratio of  
1024 periodically stratified tidal channels on the estuarine circulation, *J. Phys. Oceanogr.*, 45, 411804097,  
1025 2015.
- 1026 Scully, M. E., Geyer, W. R. and Lerczak, J. A.: The Influence of Lateral Advection on the Residual



- 1027 Estuarine Circulation: A Numerical Modeling Study of the Hudson River Estuary, *J. Phys.*  
1028 *Oceanogr.*, 39, 107-124, 10.1175/2008JPO3952.1, 2009.
- 1029 Scully, M. E., Geyer, W. R. and Lerczak, J. A.: The Influence of Lateral Advection on the Residual  
1030 Estuarine Circulation: A Numerical Modeling Study of the Hudson River Estuary, *J. Phys.*  
1031 *Oceanogr.*, 39, 107-124, 10.1175/2008JPO3952.1, 2009.
- 1032 Scully, M., Friedrichs, C. and Brubaker, J.: Control of estuarine stratification and mixing by wind-  
1033 induced straining of the estuarine density field, *Estuaries*, 28, 321-326, 10.1007/BF02693915, 2005.
- 1034 Simpson, J. H., Brown, J., Matthews, J. and Allen, G.: Tidal straining, density currents, and stirring in  
1035 the control of estuarine stratification, *Estuaries*, 13, 125-132, 10.2307/1351581, 1990.
- 1036 Van Maren, D. S., van Kessel, T., Cronin, K. and Sittoni, L.: The impact of channel deepening and  
1037 dredging on estuarine sediment concentration, *Cont. Shelf Res.*, 95, 1-14, 2015.
- 1038 Waterhouse, A., Tutak, B., Valle-Levinson, A. and Sheng, Y.: Influence of Two Tropical Storms on the  
1039 Residual Flow in a Subtropical Tidal Inlet, *Estuar. Coast.*, 36, 1037-1053, 10.1007/s12237-013-  
1040 9606-3, 2013.
- 1041 Willmott, C. J.: On the validation of models, *Phys. Geogr.*, 2, 184-194, 1981.
- 1042 Wilson, R. and Filadelfo, R. 1986. Subtidal Current Variability in the Lower Hudson Estuary. Springer -  
1043 Verlag, Berlin, Germany. p. 132-142.
- 1044 Winterwerp, J. C.: Fine sediment transport by tidal asymmetry in the high-concentrated Ems River:  
1045 indications for a regime shift in response to channel deepening, *Ocean Dynam.*, 61, 203-215, 2011.
- 1046 Zhang, R., Chen, L. H., Liu, S. S., Zhang, H. and Lin, G. Y.: Shoreline evolution in an embayed beach  
1047 adjacent to tidal inlet: The impact of anthropogenic activities, *Geomorphology*, 346, 106856, 2019.
- 1048 Zhu, J., Weisberg, R. H., Zheng, L. Y. and Han, S. Z.: Influences of Channel Deepening and Widening  
1049 on the Tidal and Nontidal Circulations of Tampa Bay, *Estuaries & Coasts*, 38, 132-150, 2015.
- 1050 Zhu, L. 2018. Alteration of estuarine circulation under the inference of morphological evolution. East  
1051 China Normal University, Shanghai, China.
- 1052